



THE HONG KONG
POLYTECHNIC UNIVERSITY

香港理工大學

Pao Yue-kong Library

包玉剛圖書館

Copyright Undertaking

This thesis is protected by copyright, with all rights reserved.

By reading and using the thesis, the reader understands and agrees to the following terms:

1. The reader will abide by the rules and legal ordinances governing copyright regarding the use of the thesis.
2. The reader will use the thesis for the purpose of research or private study only and not for distribution or further reproduction or any other purpose.
3. The reader agrees to indemnify and hold the University harmless from and against any loss, damage, cost, liability or expenses arising from copyright infringement or unauthorized usage.

IMPORTANT

If you have reasons to believe that any materials in this thesis are deemed not suitable to be distributed in this form, or a copyright owner having difficulty with the material being included in our database, please contact lbsys@polyu.edu.hk providing details. The Library will look into your claim and consider taking remedial action upon receipt of the written requests.

**OPTICAL PROPERTIES OF WS₂
DECORATED WITH GOLD
NANOPARTICLES**

CHOI SIN YUK

M.Phil

The Hong Kong Polytechnic University

2016

The Hong Kong Polytechnic University

Department of Applied Physics

**Optical Properties of WS₂ Decorated with
Gold Nanoparticles**

Choi Sin Yuk

A thesis submitted in partial fulfillment of the requirements
for the degree of Master of Philosophy

July 2015



THE HONG KONG POLYTECHNIC UNIVERSITY

Certificate of Originality

I hereby declare that this thesis is my own work and that, to the best of my knowledge and belief, it reproduces no material previously published or written, nor material that has been accepted for the award of any other degree or diploma, except where due acknowledgement has been made in the text.

_____ (Signature)

Choi Sin Yuk (Name of candidate)



Abstract

Since the discovery of graphene, two-dimensional (2D) materials have been extensively studied and shown potential applications in electronic, optical and optoelectronic devices. Atomically thin layers of transition metal dichalcogenides (TMDs) have drawn much attention due to their superb properties compared to graphene. Among TMDs, tungsten disulfide (WS_2) is one of the mostly studied 2D materials due to its fascinating properties. In this project, gold nanoparticles (AuNPs) were used to decorate 2D WS_2 crystals to tune their optical properties.

2D WS_2 was prepared by sulfurization of thin tungsten film which was deposited through the magnetron sputtering system. The surface functionality of atomically-thin WS_2 was decorated by various AuNPs. The optical properties of the decorated WS_2 layers were investigated by Raman, photoluminescence (PL) and absorption spectra. Besides, Finite Difference Time-Domain (FDTD) Solutions 8.9 from Lumerical Solutions was adapted to perform the simulated calculation in order to address the enhancement in the AuNPs/ WS_2 hybrid system.

After decoration, the enhancement of PL was exhibited by increasing the peak intensity and narrowing the peak width. Furthermore, the immersion of HAuCl_4^- could generate 8-folded PL enhancement comparing to the other two methods. In the comparison of the FDTD calculation, the PL enhancement arises from the arrangement of AuNPs pair. This is due to exciton-plasmon interaction which is highly related to spatial distribution of AuNPs, while the nucleations of Au atoms tend to form into the defective sites on the surface of WS_2 . In addition,



THE HONG KONG POLYTECHNIC UNIVERSITY

laser irradiation was employed to increase the number of defects in 2D materials in order to achieve the further enhancement of PL in the AuNPs/WS₂ hybrid system.

The decoration of AuNPs makes a change in surface functionality of 2D WS₂ such that it enhances the full width at half maximum (FWHM) of the absorption peaks and gives a slight shift to higher energy regions. These features might provide the possibility to develop potential photonic and energy harvesting applications in 2D materials. In addition, the special design of AuNPs on 2D WS₂ with different sizes, morphologies and spatial distribution would also give an effect, resulting in localized surface plasmon resonance (LSPR) interpreted in terms of surface plasmon enhanced optical properties. It can help to achieve the development for optoelectronic devices on account of the light-to-current conversion.



THE HONG KONG POLYTECHNIC UNIVERSITY

List of Publication

S. Y. Choi, C. T. Yip, G.-C. Li, D. Y. Lei, K. H. Fung, S. F. Yu and J. Hao,
"Photoluminescence enhancement in few-layer WS₂ films via Au nanoparticles."
AIP Advances **5**(6): 067148 (2015)



THE HONG KONG POLYTECHNIC UNIVERSITY

Acknowledgements

I would like to express my honest gratitude to my supervisor Dr. J. H. Hao and ex-supervisor Prof. S. F. Yu for all the supports, assistance and guidance during these study periods. Special thanks should have been devoted to Dr. K. H. Fung and Dr. C. T. Yip for their inspired discussion.

Thanks are extended to Ms S. M. Ng, Mr W. C. Wong, Dr. W. Jie and Mr. G. Bai for their assistance and helpful suggestions.

I would also like to thank the financial and technical support provided by the Department of Applied Physics and Materials Research Centre (MRC) of the Hong Kong Polytechnic University.

Last but not least, I would like to thank my family and friends for their endless love and support throughout my life.



Table of Contents

Abstract	ii
List of Publication	iv
Acknowledgements	v
Table of Contents	vi
List of Figures	ix
Chapter 1. Introduction	14
1.1. Introduction of two-dimensional materials	14
1.2. Property of 2D tungsten disulphide	15
1.3. Principle of localized surface plasmon resonance	21
1.4. Literature review of hybrid Au/WS ₂ materials	25
1.5. Motivation and scope	27
1.6. Structure of thesis	28
Chapter 2. Experimental Equipment	30
2.1. Fabrication processes	30
2.1.1. Synthesis of 2D materials	30
2.1.2. Fabrication for sulfurization of transition metal film	34
2.1.3. Thermal evaporation	36
2.2. Structural measurement techniques	38
2.2.1. Field-emission scanning electron microscopy (FE-SEM)	38
2.2.2. Atomic force microscopy (AFM)	40
2.2.3. Transmission electron microscopy (TEM)	43
	vi



THE HONG KONG POLYTECHNIC UNIVERSITY

2.3. Optical measurement techniques	46
2.3.1. Raman spectroscopy	46
2.3.2. Photoluminescence spectroscopy	48
2.3.3. Ultra-violet (UV) visible spectroscopy	50
2.4. Summary	51
Chapter 3. Fabrication and Characterizations of 2D WS₂ and AuNPs	52
3.1. Fabrication of 2D WS ₂	52
3.1.1. Sulfurization of transition metal film	52
3.1.2. Results and characterization	54
3.2. Synthesis of gold nanostructures	61
3.2.1. Seed method synthesis of AuNRs	61
3.2.2. Results and characterization	62
3.3. Experimental procedures for hybrid Au/WS ₂ structures	67
3.3.1. The formation on AuNPs/WS ₂ by HAuCl ₄ chemical solution	67
3.3.2. The preparation of AuNRs/bilayer WS ₂ hybrid nanostructure	67
3.3.3. Thermal evaporation of gold nanoparticles on WS ₂ substrate	67
3.4. Summary	68
Chapter 4. Optical and PL Properties of WS₂ Decorated with Gold Nanoparticles	70
4.1. PL enhancement via various AuNPs decorations methods	71
4.1.1. Au/WS ₂ nanostructure from HAuCl ₄ ⁻ immersion	71
4.1.2. Au/WS ₂ nanostructure from AuNRs coating	89
4.1.3. Au/WS ₂ nanostructure from AuNPs annealing	92
4.2. PL quenching from Au film/WS ₂ nanostructure	93



THE HONG KONG POLYTECHNIC UNIVERSITY

4.3. Summary	96
Chapter 5. Conclusions and Suggestions for Future Work	100
5.1. Conclusions	100
5.2. Suggestions for the future work	102
References	103



List of Figures

<i>Figure 1-1. (a) Bulk and monolayer in MoS₂. The distance between interlayers is notified by d. (b) and (c) are the side and top views of MoS₂ bulk unit cell which can be analogous with WS₂. The primitive vectors are $\mathbf{a} = (a, 0, 0)$, $\mathbf{b} = (a/2, 3a/2, 0)$ and $\mathbf{c} = (0, 0, c)$. The weak layer interaction is indicated by a spring.....</i>	<i>17</i>
<i>Figure 1-2. Schematic diagrams of the 2H and 1T - WS₂.....</i>	<i>18</i>
<i>Figure 1-3. Electronic band structure for (a) bulk and (b) monolayer WS₂.....</i>	<i>19</i>
<i>Figure 1-4. Schematic diagram showing the oscillation motion of surface charge density wave at a metal surface regarded as electron delocalization.....</i>	<i>25</i>
<i>Figure 2-1. Two kinds of routes including exfoliation and fragmentation of 2D VDW materials.....</i>	<i>31</i>
<i>Figure 2-2. The experimental setup of vapor phase deposition.....</i>	<i>33</i>
<i>Figure 2-3. The mechanism established from the substrate put into the tube furnace which is divided into five zones.....</i>	<i>33</i>
<i>Figure 2-4. The schematic diagram showing the mechanism induced by the vapor phase deposition.....</i>	<i>34</i>
<i>Figure 2-5. Working machine of ion beam sputtering.....</i>	<i>36</i>
<i>Figure 2-6. Systematic diagram of thermal evaporation system.....</i>	<i>37</i>
<i>Figure 2-7. Working principle of SEM.....</i>	<i>39</i>
<i>Figure 2-8. SEM machine.....</i>	<i>40</i>
<i>Figure 2-9. Schematic representation of (a) commercial atomic force microscopy, (b) contact mode imaging, and (c) tapping mode imaging.....</i>	<i>41</i>
<i>Figure 2-10. Atomic force microscopy.....</i>	<i>43</i>



THE HONG KONG POLYTECHNIC UNIVERSITY

<i>Figure 2-11. Working principle of TEM</i>	45
<i>Figure 2-12. TEM system</i>	45
<i>Figure 2-13. Schematic diagram of Raman scattering</i>	47
<i>Figure 2-14. Raman spectroscopy</i>	48
<i>Figure 2-15. Three mechanisms including laser pulse excitation, intra-band relaxation and recombination.</i>	49
<i>Figure 2-16. UV-visible spectroscopy</i>	51
<i>Figure 3-1. Schematic diagram of setup using for the sulfurization of TMDs materials</i>	52
<i>Figure 3-2. The calibration of deposition rate of tungsten material obtained from magnetron sputtering.</i>	53
<i>Figure 3-3. Raman spectra with respect to the monolayer, bilayer and trilayer WS₂</i>	54
<i>Figure 3-4. The corresponding PL spectra related to the monolayer, bilayer and trilayer WS₂ in Figure 3-3.</i>	56
<i>Figure 3-5. (a) Spatial distribution of photoluminescence intensity with scanning the whole WS₂ flake. (b) Spatial distribution of peak intensity's wavelength with scanning the whole WS₂. (c) PL spectra with corresponding color points in Figure (a). (d) Spatial distribution of Raman shift $\Delta\omega = A_{1g} - E'_{2g}$ with scanning the whole WS₂. All of the spectra are in μm along both x- and y-axis.</i>	57
<i>Figure 3-6. Optical microscopy from WS₂ sample fabricated by the sulfurization of thin tungsten film.</i>	58
<i>Figure 3-7. SEM image from WS₂ sample fabricated by sulfurization of thin tungsten film</i>	59
<i>Figure 3-8. TEM image from WS₂ sample. The left inset shows the selected electron area diffraction (SEAD) and the right inset shows the corresponding HRTEM image.</i>	59
<i>Figure 3-9. The EDS image</i>	60



THE HONG KONG POLYTECHNIC UNIVERSITY

Figure 3-10. AFM images from as-prepared WS_2 sample.	61
Figure 3-11. Absorption spectra of the oxidative gold nanorods during different time intervals.	63
Figure 3-12. The absorption spectrum from the gold nanorods with optimized aspect ratio.	64
Figure 3-13. The corresponding SEM image from the same experimental condition in Figure 3- 12.....	64
Figure 3-14. LMTEM image of nanorods growth.....	65
Figure 3-15. HRTEM image showing the mean aspect ratio of AuNRs is around 2.2.....	66
Figure 3-16. The prominent AuNRs aspect ratio extracted in Figure 3-14 is around 2.8.	66
Figure 4-1. PL spectra with exciton/trion emission (labeled by X/X ⁻ respectively) from (a) bare WS_2 sample and (b) Au/ WS_2 sample by Lorentzian fit in monolayer WS_2	71
Figure 4-2. PL spectra with exciton/trion emission (labeled by X/X ⁻ respectively) from (a) bare WS_2 sample and (b) Au/ WS_2 sample by Lorentzian fit in bilayer WS_2	72
Figure 4-3. Structural characterization of the synthesized nano-composites of 2D WS_2 crystals and AuNPs. (a) The Raman spectrum of a bilayer WS_2 characterized with Si substrate at 520.7 cm^{-1} . (b) The corresponding AFM image with the height profile was measured and the inset shows the SEM images with same WS_2 flake. (c) Enlarged TEM image shows the spherical AuNPs adhered onto the edge of WS_2 . (d) Low magnification TEM image with the triangular Au- WS_2 flake.	74
Figure 4-4. (a) The SEM image with labelled position 1-5 corresponding to the PL spectra obtained. (b) PL spectra of position 1-5 before and after the decoration of AuNPs. The pair of AuNPs labelled by the orange circles.	77
Figure 4-5. The model of AuNP/ WS_2 heterostructure modeled by FDTD calculation.	79
Figure 4-6. Simulated light scattering spectra including a single Au sphere with diameter of 30	



THE HONG KONG POLYTECHNIC UNIVERSITY

- nm and a pair of Au-Au sphere both with diameter of 30 nm in the spectral regions of symmetrical surface plasmon mode. 80*
- Figure 4-7. The relationship of the intensity enhancement versus interspacing between the AuNPs onto WS₂ calculated theoretically with excitation wavelength at 488 nm. 81*
- Figure 4-8. (a) Raman mapping of the intensity of the in-plane phonon mode E¹_{2g} (Γ) before doping AuNPs on the triangular WS₂ flake. (c) The upshift of peak frequency E¹_{2g} mode under the Lorentzian-fit treatment when doping AuNPs onto bilayer WS₂ crystal. (b) Raman mapping of the intensity of the out-of-plane phonon mode A_{1g} (Γ) before doping AuNPs on the triangular bilayer WS₂ crystal. (d) The upshift of peak frequency A_{1g} modes under the Lorentzian-fit treatment after AuNPs doping. The green dots straight line in (a) and (b) meaning the scanning locus across WS₂ crystal. 82*
- Figure 4-9. Spatial distribution of the PL mapping of a bilayer WS₂ (a) without Au NPs decoration and (b) the overall intensity enhancement I/I₀ comparing with and without AuNPs in the same triangle WS₂ flake. (c) and (d) are the spatial distribution of the peak position mapping of a bilayer WS₂ from (a) and (b). 83*
- Figure 4-10. (a) and (b) showing the absolute optical absorption spectra of the same bilayer WS₂ flake with labelled excitons I and A representing indirect and direct emission energies from WS₂ crystal with and without AuNPs coating measured at room temperature. The inset of (b) showing the absorbance enhancement in existence of AuNPs. (c) The average PL intensity enhancement extracted from Figure 4-9 (a) and (b). (d) The diameter of Au NPs size distribution estimated by TEM image. 85*
- Figure 4-11. The variation of absorption intensity and energies before and after AuNPs decoration. 86*
- Figure 4-12. (a) Raman spectrum of the same bilayer WS₂ from the Figure 4-3 before (black line)*



THE HONG KONG POLYTECHNIC UNIVERSITY

and after (red line) decoration of AuNPs. This spectrum collected by 488 nm excitation wavelength. The inset showing the enlarged graph of the splitting Raman mode E'_{2g} with Lorentzian fit. (b) The statistical distribution of average PL enhancement from total 32 Au- WS_2 flakes..... 87

Figure 4-13. AFM image of AuNR/bilayer WS_2 with height profile along with the labelled scanning axis. 89

Figure 4-14. Spatial distribution of the PL mapping of a bilayer WS_2 (a) before and (b) after Au NPs decoration..... 90

Figure 4-15. SEM characterization. 91

Figure 4-16. (a) Spatial distribution of the PL mapping of a bilayer WS_2 (a) before and (b) after Au NPs annealing. (c) SEM images characterization. (d) The enlarged image captured by SEM..... 92

Figure 4-17. Raman spectrum of Au/ WS_2 hybrid system with a labelled Si peak as a reference. The inset showing the OM image of the as-prepared Au/ WS_2 system. 93

Figure 4-18. The PL spectra corresponding to WS_2 , Au/ WS_2 and Au film. The inset showing the enlarged PL spectra of Au film and Au/ WS_2 heterostructure ranging from 580 nm to 800 nm, respectively..... 94

Figure 4-19. High resolution AFM image of Au film on Si substrate. 95

Figure 4-20. Energy band diagrams of Au/ WS_2 (a) and (b) showing the electron transfer mechanism in hybrid Au/ WS_2 system before and after contact establishments respectively. 96



Chapter 1. Introduction

1.1. Introduction of two-dimensional materials

Two-dimensional (2D) materials have been rapidly developed from the first decade in 21 century and have caused much attention on the research communities. It is because the extremely thin materials down to the unit cell thickness will thermally fluctuate in a unit lattice so as to induce a thermodynamically instability at whatever temperature in the classical physics explanation [1]. The prototypes of 2D materials typically possess a 3D layered structure such as graphite and molybdenum disulfides. Mermin had been proven that the exfoliation can produce 2D monolayer materials theoretically based on their domain within the harmonic approximation [2]. In 2004, Novoselov and Geim gave a surprising breakthrough in successful isolation of graphene via mechanical exfoliation by scotch tape [3]. The semi-metal graphene has a honeycomb structure composed of single layer sp^2 carbon atoms as well as a zero-bandgap. It shows a high stability evidenced by the 25% strengthening of three C-C bonds in graphene comparison to that of four C-C bonds in diamond. Within the Brillouin zone, it shows linear dispersion relation at K points. A novel character manifests a zero effective masses of electrons and holes and hence gives a high current density. Such kind of fascinating properties including supreme electron mobility in finite temperature and the lowest spin-orbit interaction, can make it immense advances in spintronics [4]. However, the no/low band gap character of graphene is not favor in development towards electronic and optoelectronic applications.



1.2. Property of 2D tungsten disulphide

Besides graphene, Frindt et al. discovered the 2D layered materials classified as the nature of interaction between layers [5-8]. Those interactions include hydrogen bonds, interstitial cations and London dispersion between layers. The novel 2D materials beyond graphene are the transition metal dichalcogenides (TMDs) in which MoS₂ is a representative example [9, 10]. The reason for the low on/off switching performance in graphene-based field effect transistor [14] owing to the lack of band gap [15] starts turning researcher eye on the 2D TMDs family. The atomic structure of MoS₂, analogue to that of WS₂, is shown in Figure 1-1. Figure 1-1 (a) and (b) show the bulk and monolayer MoS₂ as well as the side and top views of the MoS₂, respectively. Some exfoliation techniques including ion intercalation, mechanical and chemical cleavages, and surfactant-assisted ultra-sonication can isolate the bulk TMDs materials into single or few atomic layers. Scientists have interests in developing 2D MoS₂ based transistors for ultrathin and flexible devices as well as for other nanoelectronic and optoelectronic applications [11, 12].

At the early stage of discovery, researchers mainly focused on the attempt of fabrication and characterization of those 2D materials. Many techniques such as transfers, characterization, synthesis and manipulation are applied on TMDs materials which were yielded during the graphene researches. Also, well-known synthetic methods including solvothermal, solution-based and ultra-high vacuum (UHV) surface epitaxial approaches have innovated to create 2D TMDs materials in a fast pace of invention [13].

The TMDs are MX₂ type's compounds in which M is symbolized



THE HONG KONG POLYTECHNIC UNIVERSITY

transition metal species from groups IV, V and VI in periodic table and X is representing those chalcogen species including S, Se and Te etc. There are various combinations between different kinds of transition metal species and chalcogen species. In the TMDs family, the materials can be semiconductors, metals as well as superconductors highly related to their own crystal structures. WS_2 as one of the popular representatives in TMDs family belongs to a different class of 2D materials due to the new physics arising from linear combination of tungsten d-orbital electrons interacting with p_z -orbitals in sulfur [22]. In monolayer WS_2 , the transition metal atom W is sandwiched by two trigonal coordinated sulfur atoms holding by intra-covalent bonds to form a hexagonal crystal structure as shown in Figure 1-1 (c). In general, the monolayer WS_2 has been hold in between the weak Van der Waal's (VDW's) interaction in the stacking layered structure to form bulk crystal [23]. The metallic octahedral (1T- WS_2) and semiconducting trigonal crystal structures (2H- WS_2) shown in Figure 1-2 (a) and (b) are most commonly formed in WS_2 . In 2H- WS_2 crystalline structure, the lattice parameters of a and c are 3.1532 Å and 12.323 Å, respectively [24].

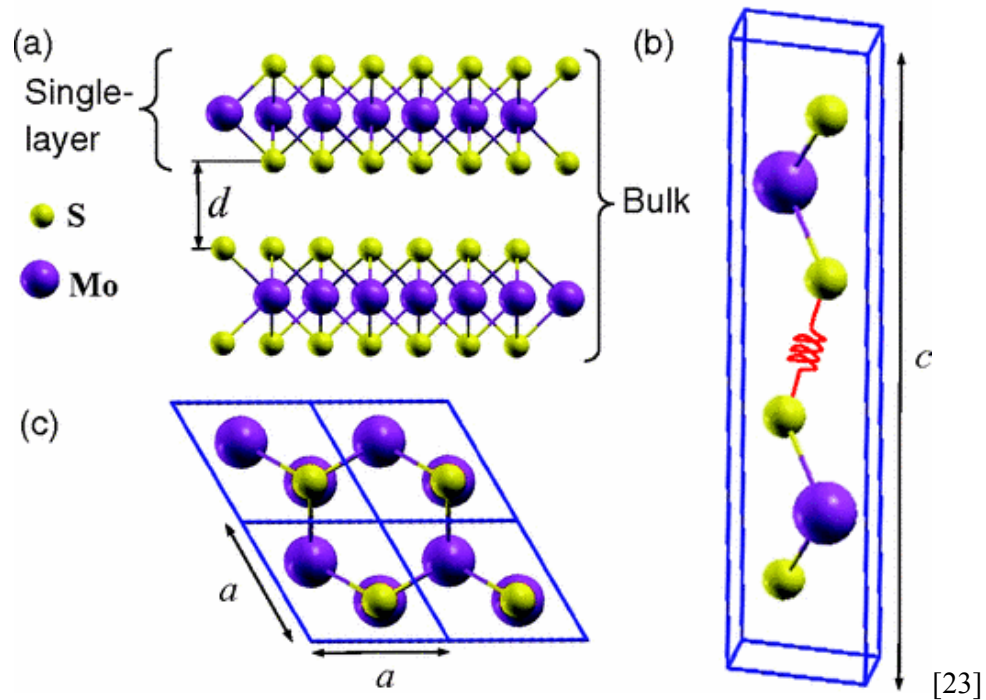


Figure 1-1. (a) Bulk and monolayer in MoS₂. The distance between interlayers is notified by d . (b) and (c) are the side and top views of MoS₂ bulk unit cell which can be analogous with WS₂. The primitive vectors are $\mathbf{a} = (a, 0, 0)$, $\mathbf{b} = (a/2, \sqrt{3}a/2, 0)$ and $\mathbf{c} = (0, 0, c)$. The weak layer interaction is indicated by a spring. [23]

The electronic states are strongly related to the number of layers in which there is great intra-layer coupling in those electronic states. From the individual layer, the features of indirect energy-band gap are larger than the direct transition at K point, which can generate direct band-gap semiconductor of monolayer WS₂. These particular properties in monolayer push ahead the application platform in optoelectronics [25] and valleytronics [26, 27]. Of course, monolayer WS₂ still has much attractive properties such as magnetism [28], charge density waves [29] and superconductivity [30] going on in research's exploration. The coulomb interaction of WS₂ is intensely strengthened in monolayer in which the excitons predominate the charge-transport as well as optical properties [31]. The single

layer is reported in 0.92 nm thick [32]. Besides, the act of weak VDW's force between layers can produce a hetero-structure from various TMDs materials without concerning the lattice matching problems.

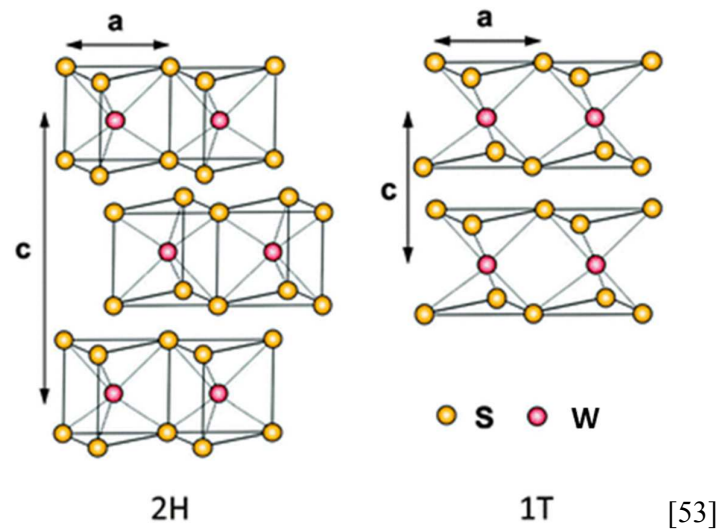


Figure 1-2. Schematic diagrams of the 2H and 1T - WS₂.

It is noteworthy that WS₂ crystal has layer-dependence tunable band-gap energy due to the quantum confinement effect [33, 34]. The band-gap energy of WS₂ transits from indirect 1.3 eV in bulk structure (valence band maximum at Γ point to conduction band minimum at T point) to direct 2.1 eV in monolayer crystal shown in Figure 1-3. Figure 1-3 (a) and (b) are representing electronic band structures in bulk and monolayer WS₂ respectively. This is a valuable investigation for the small change in valence band at K point for bulk and monolayer WS₂. In monolayer form such as 2D materials prototype MoS₂, the spin-orbit arisen valence band splitting to doubly degenerate conduction band will lead to two possible direct transitions at K point in Brillouin zone [35, 36]. This

transition features were observed by the absorption spectroscopy allocated the exciton A (1.95 eV) and exciton B (2.36 eV) [37]. Due to lack of splitting in valance band, the monolayer WS₂ only reveals a direct electronic transition by optical spectroscopy. Also, due to the reduction in effective mass, monolayer WS₂ supposed to have the higher mobility (~ 140 cm²/Vs at low temperature and above ~ 300 cm²/Vs in bilayer) [38]. It also has a high on/off current ratio at room-temperature at about $\sim 10^6$. Because of the large mass of tungsten atom, the valence band splitting induced by spin-orbit coupling in WS₂ is three times larger (≈ 426 meV) than that of MoS₂ and give an obvious valley hall effect. Also, the outstanding ambipolar behavior of WS₂ lets both electrons and holes are transported [25, 39].

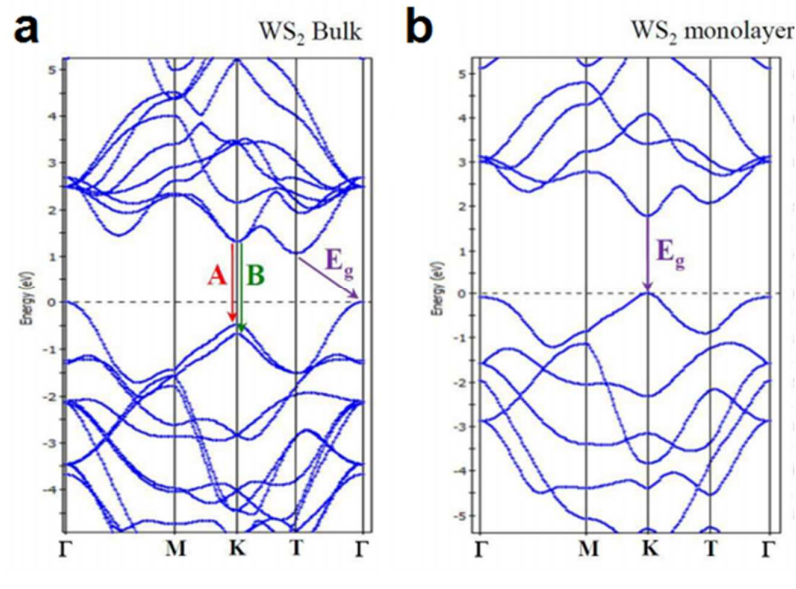


Figure 1-3. Electronic band structure for (a) bulk and (b) monolayer WS₂.

The fabrications of few-layered semiconducting WS₂ crystals have



experimentally achieved via mechanical exfoliation from the bulk form [35, 36, 40], wet chemical approaches [8, 41, 42], physical vapor deposition [43] and sulfurization of transition metal film [44, 45]. Here the fabrication of mono- to few- layered WS_2 crystals would be adopted for sulfurization of transition metal tungsten film. From the previous reported [46], various forms of WS_2 such as nanotube and fullerene-like structures were possibly been synthesized. The monolayer WS_2 crystals with direct band gap have interesting light emission properties in visible and near-infrared regions. This kind of intermediate behavior favors the possible optoelectronic applications such as photo-detector [47, 48], photovoltaic solar cell [49] and their photo-catalytic applications due to its strong absorption in the solar spectrum region [50]. In the previous reports [22, 51, 52], the photoluminescence (PL) intensity of WS_2 prepared by chemical vapor deposition (CVD) increased with decreasing number of layers. As the results of direct band-gap in monolayer, that triangular WS_2 will emit an intense red luminescence as well as the attenuation of light emission from the edge towards the body center gradually. The light emission will be strengthened on the edge compared to that of center [51, 52]. Not only the intensity of triangle WS_2 , but also the peak width and position give a variation from emission. However, the overall PL from exfoliated WS_2 is comparable to that from CVD methods. From the pioneering works [52], growth of WS_2 by different experimental conditions is possible to produce non-uniform and uniform PL in the whole triangle WS_2 . Non-uniform PL gives features in quenching and blue-shift in the body center of triangle WS_2 as well as the extraordinary PL in the edge which are possibly due to the structural flaw or n-type doping by charge defects. Nevertheless, the



uniform PL features intense, intrinsic and non-blinking highly related to crystalline structure.

1.3. Principle of localized surface plasmon resonance

According to the previous reports [54-56], the explanation of localized surface plasmon resonance (LSPR) is the charge density oscillations restricted on the metallic nanoparticles (NPs) and nanostructures. Once the sizes of conductive NPs are much smaller than that of incident light wavelength, for example, $R/\lambda < 0.1$, where R is the radius of NPs and λ is the wavelength of incident light, the oscillating electric field would induce the oscillations of surface electrons from the conduction band and produce excitation of LSPR. Therefore, the electric charges will be polarized and accumulated onto the surface of NPs. This interaction leads to the strong light scattering, forming high intense surface plasmon absorption bands and enhanced local electromagnetic fields. The resonant frequency from the charge oscillation and the intensity of surface plasmon absorption bands are the features of different kinds of materials. In general, the features include the bandwidth, peak intensity, the energy of the maximum absorption related to the parameters including sizes, size distribution, surface coverage, as well as the environment surrounding the nanostructure [57-59]. Au and Ag are common utilized materials due to the energy level transition from $d-d$ orbital responsible for the visible light region [60]. The optical properties of NPs differ from that of bulk because of the low dimensionality down to the quantum scale. Changes of the dimension would make the continuous energy level become discrete. Figure 1-4 shows the oscillation of the surface charge density



wave at a metal surface regarded as electron delocalization when electric field excited on the metal nanoparticles (MNP). Also, when dimensions of NPs are much smaller than the wavelength of exciting light, it reveals that there are broad and intense absorption bands in visible region. As the literature mentioned [61], Gustav Mie is the first researcher who observed the strong intensity color from dispersed colloidal gold particles in 1908. In the classical Mie theory, the homogeneity in between nanoparticles and surrounding medium assumed expresses by bulk optical dielectric function [62]. By solving the Maxwell equation, the overall extinction cross-section is equal to the summation of absorption cross-sections and scattering cross-sections for metallic particles by counting all electric and magnetic field oscillation. When the incident wavelength is much longer than the radius of nanoparticles, the equation of Mie theory can be reduced as below [57]:

$$\sigma_{ext}(\omega) = 9 \frac{\omega}{c} \epsilon_{3/2} V_0 \frac{\epsilon_2(\omega)}{[\epsilon_1(\omega) + 2\epsilon_m]^2 + \epsilon_2(\omega)^2} \quad (1)$$

where $V_0 = (4\pi/3)R^3$, ω is the angular frequency of excitation radiation, ϵ_1 and ϵ_2 represent the real part and imaginal part of dielectric function surrounding metal nanoparticles respectively. From Equation (1), when the imaginary part of dielectric function of the metal nanoparticles is less dependent on the angular frequency, in which $\epsilon_1(\omega)$ is approximately equal to $-2\epsilon_m$. The bandwidth and peak intensity of surface plasmon absorption band would be predicted by $\epsilon_2(\omega)$. However, no evidence shows the relationship between the size and peak wavelength from the Equation 1. Also, Equation 1 is not suitable for explanation of optical behavior in those metallic NPs with diameter larger than 30 nm. The extinction cross section in those larger metallic NPs is predominated by high-



order multipole absorptions and scatterings in full Mie theory [63, 64]. By Free-electron behavior in Mie equation supported with Drude's theory, the relationship between metallic NPs sizes and surface plasmon band can be established rationally [57, 65]. However, Mie theory can only be applicable for well-dispersed nanoparticles with low concentration. When those nanoparticles are closely packed, it will reveal red-shift in lower energy absorption band resulting from the plasmon resonance similar to the longitudinal mode of absorption band attributed to the nanorods structure. In the separations between the arrayed metallic NPs, both near field coupling and far-field dipolar interactions occur when particles are nearly touching. The electrodynamic dipolar interactions induce plasmon oscillation of a single particle which in turn induces a surface plasmon oscillation in adjacent particles. Nanoparticle coupling in dipole modes is able to induce a strong red-shifted dipole-active mode for external field orientation along the inter-particle axis and a blue-shifted mode for perpendicular orientations [66-68]. The far-field dipolar interaction was investigated by utilizing the patterned nanoparticles as waveguides [69, 70].

Besides the explanation of surface plasmon resonance by a single NP, it would be deviated from altering the separations between the dimers. By varying the interspacing between dimers, different distinct behaviors were correlated in three regimes [71]. First, when the dimers are widely separated, it could be regarded as no interaction between them except that the interfered oscillation induced by the response of inter-particle separation which is comparable to their wavelengths. When the dimensionality of particles is smaller than wavelength, the interference effect would be suppressed but not for the inter-particle coupling. The



gradual reduction of dimers separation gives red-shift in dipolar mode. The reductions of the effective dipoles from the dimers initialize the deterioration of the far-field interaction [71]. Decreasing the dimers separation continues the red-shifting and near-field enhancement resulting from the charge building up at the gap. Thus, the far-field scattering would recover. The other two regimes in theoretical cases are neighboring separated dimers nearly touching and the dimers overlap respectively. The literature has ever been described about the situation in which particles are in nearly-touching boundary [72]. In that situation it would induce intense modes causing a shift towards infrared region when coming in touching. However, the results would be reversed when particles' started overlapping. There was a discontinuous evolution on the situation in which the particles were just in touching each other. The limitation of nearly touching dimers induced four possible situations in troubles, for examples, tremendous enhancement in electric field arisen from the maximized closely-spaced nanoparticles [73, 74], the plasmon resonance shifted towards infrared [67, 68, 75], the modes vanishing or appearing by particles nearly touching [67], and singular transition due to particles touching [67]. However, researchers have already focused on studies about both interaction between the near separated nanospheres in non-retarded limit [67, 68, 76-82] and full retardation effect [71-73, 83-85].

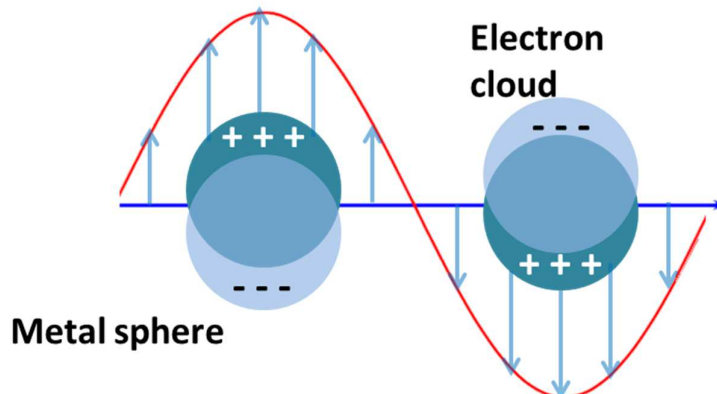


Figure 1-4. Schematic diagram showing the oscillation motion of surface charge density wave at a metal surface regarded as electron delocalization.

1.4. Literature review of hybrid Au/WS₂ materials

The description of the decorating MNPs on 2D materials from scientists is one of the popular ways to modify their surface functionality [86]. It also gives an improvement on properties in a certain regions such as energy storage and catalysis [87-91]. By tackling the MNPs decoration onto 2D materials, both mixing individual components and adding TMDs sheets into mixtures including metal precursors as well as reducing agents would be adopted [92-95]. From the previous reports, the TMDs materials could have spontaneous reaction with those metal precursors such as hexachloroauric acid (HAuCl₄) in water to form well decorated TMCs nanostructures especially along the defective sites including edges and the grain boundary in the basal planes [88]. Those structures with conductive MNPs could boost the charge transportation between the planar directions and as the spacers to further hinder the restacking of 2D TMDs sheets when using chemical exfoliated TMDs sheets. The formation of stable binding



sulfur-noble MNPs in hybrid AuNP/MoS₂ or AuNP/WS₂ nanostructures would be incorporated to improve the efficiency of gate-voltage in an order of magnitude as well as the Hydrogen evolution reactions (HERs) significantly [96, 97]. Also, the other approaches to fabricate hybrid AuNP/MoS₂ structure via both reaction arresting by microwave and diffusive limited aggregation on the crystallographic defects from TMDs crystals make an angular deposition 60°C [86]. After surface functionality, it raises the capacitive interactions between MoS₂ and AuNPs in electrical, thermal and Raman enhancements such as lower Schottky barrier in 14.52 meV, a reduced thermal barrier in carrier transport in a range of 253 to 44.18 meV, an improved thermal conductivity from 15 to 23 W/mK and capacitance in 2.17 $\mu\text{F}/\text{cm}^2$ [86]. The optical properties of hybrid plasmon-excitonic nanostructure originated from monolayer MoS₂ coating with gold nano-antennas have been investigated by spatial resolution PL spectroscopy [98, 99]. Two resolved in- and off-resonance from plasmonic-excitonic luminescence analyzed in the direction parallel and perpendicular to the antenna long axis for non-polarized excitations give distinguishable features respectively. For the plasmonic pumping, it gives 65% intensity enhancement in PL resulting from the influences of surface plasmons [99]. In addition, the interesting physical properties such as generation of local mechanical strain are also formed in hybrid AgNP/MoS₂ nanostructure [100]. The exploitation of enhanced local field at boundaries between MNPs and TMDs layers as a result of Surface Plasmon enhanced Raman Scattering (SERS). The strong evidences given that both the in-plane Raman active mode E_{12g}^1 and out-of-plane A_{1g} mode are split in monolayer MoS₂ but weaken in the layer as thick as possible. Also the prohibited E_{1g} mode from



backscattering Raman process has been initialized by the localized mechanical strain. And hence the optical transitions from indirect band gap in which the number of layers > 2 has been quenched. Besides, the electronic and phonon structures have been modified after MNPs deposition to affect the electrical transport through metal–MX₂ contact. The shoulder of PL peaks in MoS₂ becomes broader and softer in comparison to the original direct optical bandgap transition peak. Moreover, the electronic structure of hybrid system from Au nanoislands evaporated onto MoS₂ would also be quenched which is due to charge transfers from MoS₂ to Au causing the p-type effect [101].

1.5. Motivation and scope

The unique properties of 2D materials have attracted many scientists' attentions since the discovery of graphene. Some of the scientists have put much attention to the low dimensional modification in metal-2D semiconductor hybrid composites such as electrical, electro-catalytic [88], thermal and especially optical properties [86, 101, 102] due to electron transfer through metal-semiconductor contact attributed on energy-band bending. In this work, we will focus on the modification of optical emission which can be divided into PL quenching [101, 103] and PL enhancement associated with exciton/trion recombination in semiconducting TMDs materials [104, 105]. The interaction of optical excitation from tunable optical properties resonance is related to surface plasmon from MNP and low dimensionality of semiconducting induced quantum confinement effect [106]. Transition due to the optical excitation occurring in the electronic levels in semiconductor becomes discrete in the conduction and valance band, and can be



tunable by different sizes and sharp of MNPs in order to modify the PL emission from neutral excitons (X) and negatively charged exciton called trions (X^-) [104]. The formation of quasi-particles X^- composes of two electrons and a hole found in two dimensional semiconducting crystals MoS_2 . It generally reveals the dominant exciton peak with lower energy resonances. Those bound electrons giving a collective oscillation in the conduction band are called surface plasmon forming dielectric difference between MNPs and non-conductive surrounding medium so as to induce the phenomenon called exciton-plasmon coupling. In this thesis, we try to modify the sizes of MNPs and tune the separation between gold nanoparticles in order to investigate the PL enhancement in AuNP/WS_2 nanostructures. By considering LSPR effect on the hetero-structure of Au/WS_2 nanostructure, this thesis shows the attempt on the investigation of the exciton-plasmon coupling by designing a new configuration of AuNPs onto bilayer WS_2 so as to induce a PL enhancement in the relatively new semiconducting materials of WS_2 crystal. Through various characterizations such as optical absorption, PL, and photoconductivity spectroscopy, it is clear to observe the resonant frequency of synthesized AuNPs and the structure of AuNP/WS_2 causing to the enhancement/quenching via decorating AuNPs onto WS_2 .

1.6. Structure of thesis

The sequence of the thesis arrangement is as the following described:

In Chapter one, a brief introduction on 2D materials is shown and the currently useful synthesized methods and physical properties for WS_2 are



summarized. Then an elaboration on the principle of surface plasmon resonance (SPR) is introduced. Furthermore, the literature review is presented on various 2D semiconducting TMDs materials cooperated with metal nanoparticles.

In Chapter two, equipment related to both fabricating the ultrathin WS₂ as well as characterizing the structural morphology and optical properties of WS₂ are introduced subsequently.

After that, Chapter three includes the summarized experimental conditions on the fabrication process of tungsten disulfide, chemical synthesis of gold nanorods with desired aspect ratio and gold nanoparticles prepared by the immersion of HAuCl₄. Then the relevant characterization and measurements related to the as-prepared 2D WS₂ are performed.

Chapter four is the main results and data analysis related to the fabricated hybrid Au/WS₂ nanostructure with different gold morphologies nanostructures in thin film and nanoparticles and stacking sequences with WS₂. The influence factors of the PL enhancement or quenching are discussed subsequently.

Chapter five is about the conclusions and suggestions for the future work.



Chapter 2. Experimental Equipment

This chapter provides an introduction of fabrication methods in 2D materials as well as those characterizations techniques used in this project. It is divided into three sections, including synthesis process of 2D materials, fabrication of thin film and used equipment for characterizations of 2D materials in structural morphology and optical measurements.

2.1. Fabrication processes

2.1.1. Synthesis of 2D materials

❖ Mechanical exfoliation

Those two-dimensional materials such as graphene and in TMDs family with VDW's layered structure can be prepared by mechanical exfoliation. With regarded to top-bottom concept, the monolayer can be achieved from peeling off the bulk materials in layers. The VDW's force interactions needed to be overcome between the adjacent layers of 2D material flakes. We can apply two different kinds of forces in lateral and normal directions during the exfoliation. The normal force is to overcome the VDW's interaction to separate the layers apart via the micromechanical cleavage by Scotch tape. The 2D materials with lubricant ability can exert the lateral force to drive the relative motions layer by layer. These two mechanical routes are preliminarily required for the fabrication of 2D materials [107]. The other method is the additional route appeared in the fragmentation effect during mechanical exfoliation. The larger pieces of bulk crystals or particles undergoing exfoliated will be splintered into many small pieces due to the forces

reduced in lateral sizes materials. It is not effective for large area 2D materials exfoliation. However, the small fragments are easy to do exfoliation than larger one due to the smaller collective VDW interactions between layers needed to be controlled.

Figure 2-1 illustrates two different exfoliation routes for mechanical exfoliation and fragmentation of the small flakes or particles from 2D materials.

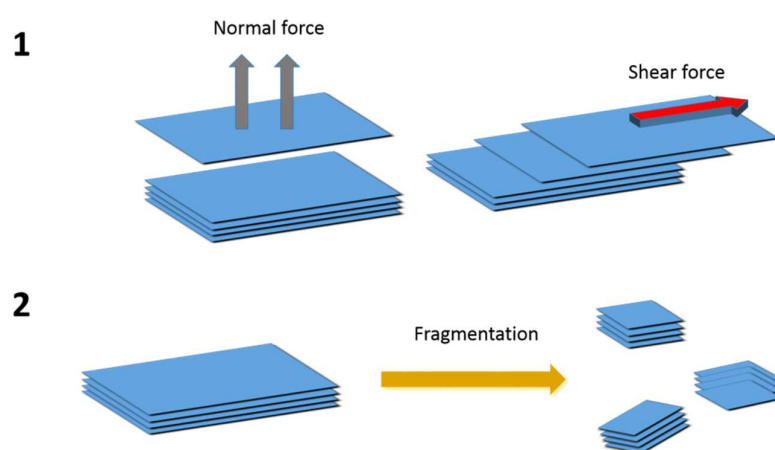


Figure 2-1. Two kinds of routes including exfoliation and fragmentation of 2D VDW materials.

❖ Vapor phase deposition

Vapor phase deposition occurs when precursors are chemically reacted in the vicinity of the heated substrate with thermal energy. It includes vapor phase transport and recrystallization which is CVD and sulfurization of metal thin film. The products can be regarded as coating, powders form and crystals. In the process, the carrier gases with reactant's vapors flow over the heated surface of substrate. The experimental setup was shown in Figure 2-2. A sufficiently high vapor



pressure is essential to mix the vapor phases of precursor components so as to transport the reactants onto the substrate. An adequate molecular stability of the precursor vapor is needed to avoid decomposition of the precursor or premature reaction. Due to the gas flow and temperature applied during vapor phase deposition process, five reaction zones would be established to induce mutual interaction so that the finalized products will be obtained in Figure 2-3. Due to the fluid dynamics, stagnant boundary layers appear adjacent to the substrate and are coated in vapors. The transport of gaseous reactants and products will come across these layers during depositions. The homogeneous reaction in zone 1 leads to flaky and less adhered coating from the undesired homogeneous nucleation. In the situation without homogeneous reaction, its reaction might be favorable. The heterogeneous reactions would appear at the interface between stagnant layers in vapors and coating. The deposition rates and properties of coating are determined by these heterogeneous reactions. The temperature would control the solid state reactions, such as recrystallization, grain growth, precipitation and phase transformation in zone 3-5. The diffusion region in zone 4 would form intermediate phases and affect the adhesion property between the coating and substrate [108]. Figure 2-4 shows the schematic diagram of the gas flow and the atomic scale chemical environment in the region of the growing film surface during the vapor phase deposition process.

There are several experimental conditions affecting the formation of products, such as composition of reaction gas mixture, pressure in the quartz tube, substrate materials, temperature applied and composition of gaseous reactants.



Figure 2-2. The experimental setup of vapor phase deposition.

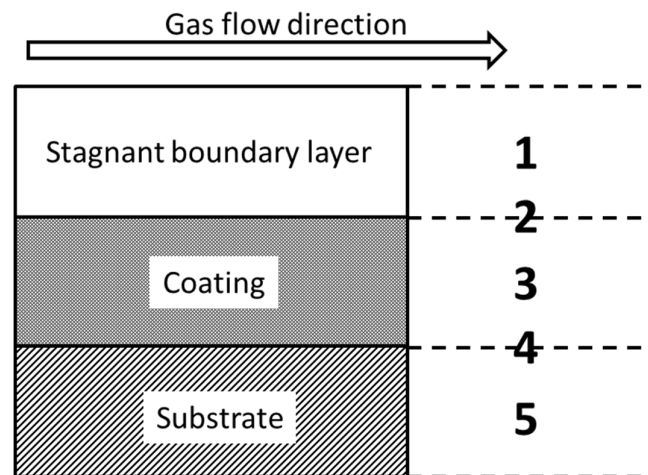


Figure 2-3. The mechanism established from the substrate put into the tube furnace which is divided into five zones.

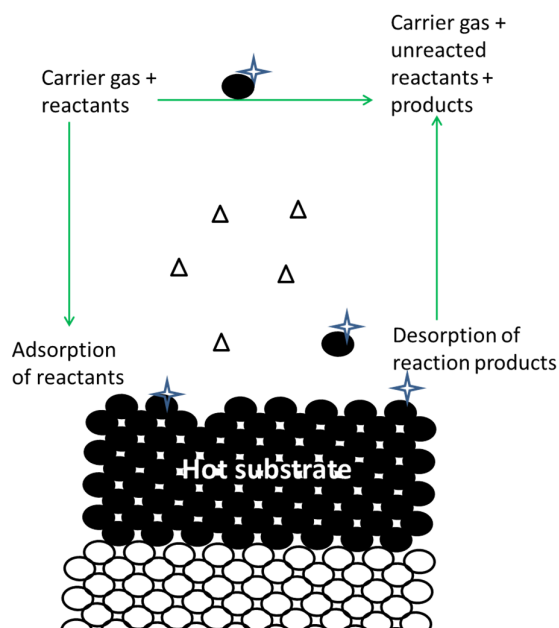


Figure 2-4. The schematic diagram showing the mechanism induced by the vapor phase deposition.

❖ Summary

There are many fabrication methods for producing 2D materials. This part only gives a brief description in the mechanism on mechanical exfoliation and vapor phase deposition respectively. It is due to mechanical exfoliation is the initialized method in advances on the preliminary demonstration on monolayer in this world and the vapor phase deposition method is the well mature methods for developing successful fabrication of large-area 2D materials nowadays.

2.1.2. Fabrication for sulfurization of transition metal film

❖ Magnetron sputtering

Sputtering is one of the film deposition methods dependent on the establishment of d.c discharge present between the surface of target and the



substrate. It is complicated to carry out the experiment although the experimental setup involved in Figure 2-5 is simply. During the discharge process, the energetically positive ions are released by argon gas molecules hitting on the target placed to cathode. This target will gain momentum transferred from collisions of positive ions and start to dispersion. According to the simple principle of sputtering, it should not involve any chemical reactions. The average velocities of the sputtered atoms are relatively high comparing to velocities of thermal evaporation target when reaching the substrate. As a result of high kinetic energies of sputtered atoms, they might lead to penetration through the surface of substrate with the depth about centimeters and it has a chance for abandon of those damaged substrates. The experiment is conducted under the level of pressures at about tenth order of Torr. There was large controversy existing when different compositions of films produced by sputtering with various physical properties were measured in the past. This is due to the impurities in carrier gas. However, the recent chamber is pumped out until the high vacuum level is achieved to ensure the use of high purity of carrier gas during sputtering. Therefore the efficiency of film production becomes more reliable [109, 110].

In this project, sputtering is used to produce a thin layer of tungsten film in order to fabricate the two-dimensional semiconducting WS₂ flakes by sulfurization of thin tungsten film.



Figure 2-5. Working machine of ion beam sputtering

2.1.3. Thermal evaporation

One of physical vapor deposition methods is thermal evaporation. The corresponding systematic diagram is shown in Figure 2-6. This is a vacuum deposition technique for thin film fabrication or applying coating of metals on the surfaces of various materials. An electric resistance heater was used to melt the source materials by receiving adequate thermal energy in the evacuated chamber. And then those materials will be evaporated at the suitable vapor pressure. All the vapors undergo solid-state condensation from the evaporated sources reaching substrate without any reaction or scattering against other gaseous phase atoms.

Any impurity from the residual gas will be pumped down by the turbo before evaporation. The key advantage from using thermal evaporator is that it is the simply method for film deposition. In addition, it is cheap; less damage on the sample surface and produces high purity of the film. However, the major disadvantage is that it will cause a majority of wastes without recycling from the source materials during the process. It is not possible to evaporate the dielectric materials. Also, the size of filament gives limitation on the deposition by amount of sources and poor densities as well as the adhesion are needed to improve. Another disadvantage is the limitation of the usage of high melting point materials. In order to modify the film qualities, the vacuum of the chamber and purity of the source materials can be adjusted. The geometry of the chamber can vary the thickness of the film deposition [111].

After fabricating Au islands by placing less amount of Au wire, it will be followed in the annealing by tube furnace to aggregate the AuNPs [111].

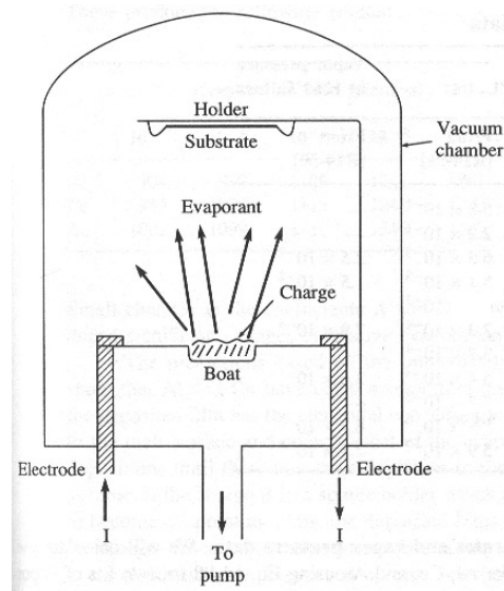


Figure 2-6. Systematic diagram of thermal evaporation system.



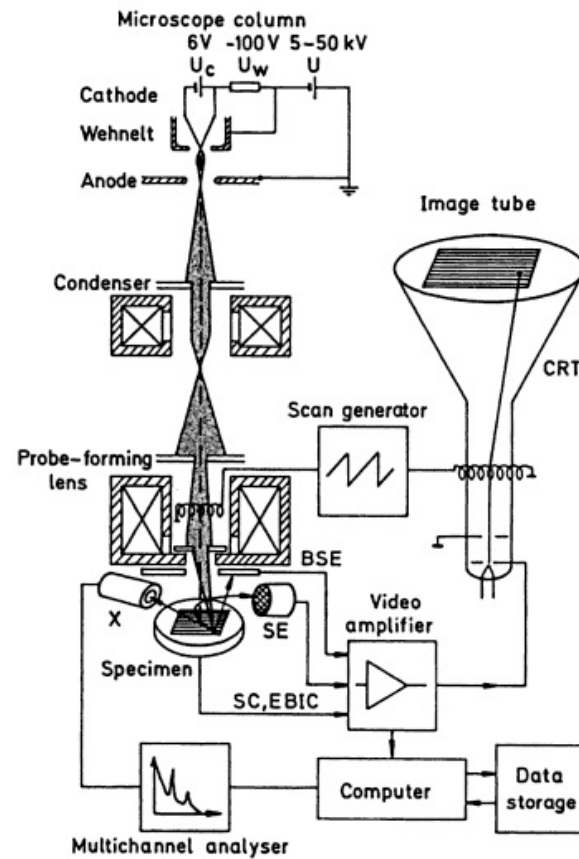
2.2. Structural measurement techniques

2.2.1. Field-emission scanning electron microscopy (FE-SEM)

FE-SEM was utilized to observe the microscopic unit of the specimens with the upper limit of magnification falling in the range of 25 X to 500,000 X. The structure of specimens larger than micrometers in diameter cannot be observed by FE-SEM clearly because of the diffraction of the visible light.

There is an electron gun produced an electron beam towards the surface of the specimen with a working potentials between 0.1 keV to 30 keV. Low voltage scanning electron microscope (LVSEM) works within the range 0.1 eV to 5 keV. By using the LVSEM, there are many advantages. For examples, collection of the information from the depth of the specimens can be improved within a few nanometers, reduction of charging the specimens during working process, reduces the damage of biological samples and semiconductors, and enhancement of the field of secondary electrons.

The principle of FE-SEM is that electron gun emits an electron beam and hits on the surface of the specimens, as shown in schematic diagram of FE-SEM in Figure 2-7. There are a few different electrons scattered from the specimens such as backscattered electrons (BSE), secondary electrons (SE) and X-ray (X). When the electron beam hitting the specimens, there are electron-beam-induced current (EBIC) and the specimen current are formed. All parameters are amplified by the video amplifier and those signals will be sent to image tube, then the image will be formed in Figure 2-7 [112]. Figure 2-8 is the instrumentation setup of SEM.



[112]

Figure 2-7. Working principle of SEM

In this project, SEM is used to observe the morphologies of WS_2 . The working voltage of the SEM is 5 keV, which belongs to the operation range of LVSEM. And the electron-probe current is 10^{-12} A.



Figure 2-8. SEM machine

2.2.2. Atomic force microscopy (AFM)

AFM is able to provide 3D profile of the sample surface at nanoscale by measuring the forces in the probe-sample separation within 0.2 to 10 nm. The probe is placed on the end of cantilever when AFM tips touching the sample surface lightly. After that, the forces will be recorded due to the change in the stiffness of cantilever which is between the probe and the sample surface. The relationship of the force can be expressed by Hooke's law [113]:

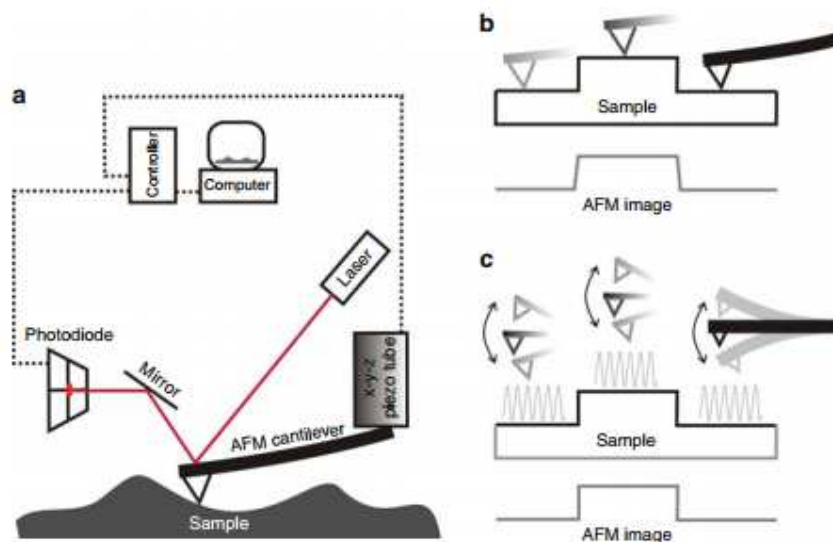
$$F = -k * x \quad (2)$$

where k is the spring constant and x is the deflection of cantilever.

The usual probe materials are made from Si_3N_4 or Si. These materials have different spring constants and resonant frequencies dependent on materials, length of cantilever and shapes. Also, the probe can be coated with other materials for other SPM applications, such as chemical force microscopy (CFM) and magnetic force microscopy (MFM).

The typical spring constant of cantilever is 0.1-1 N/m and the force ranging is from nN to μN in atmosphere. In the control of the probe movement is from the feedback loop and piezoelectric scanners, measurement of deflection from the probe can be done by “beam bounce” method.

A semiconductor diode beam is reflected off from the back of cantilever to the photo-diode detector which is sensitive in changes of positions. While the tip is scanning over the surface of samples, the cantilever will be deflected to change the position of diode beam and surface topography can be obtained.



[113]

Figure 2-9. Schematic representation of (a) commercial atomic force microscopy, (b) contact mode imaging, and (c) tapping mode imaging.



There is VDW's interaction presence due to the short probe-to-sample separation in AFM. When the tip is contacted with the surfaces of sample, the probe will dominate a repulsive VDW's force. While the tip is a little bit away from samples, attractive VDW's force is dominated. It can be divided into three different modes of AFM operations, including contact AFM, tapping mode AFM and non-contact AFM shown in Figure 2-9 (a), (b) and (c) which represent different modes of AFM [113].

Three modes of AFM associated with different advantages and disadvantages. In contact mode AFM, keeping the same deflection of the cantilever by feedback loop, the forces between sample and probe will be the same so as to obtain the image on the sample surface. It leads to fast scanning on a rough surface by analyzing the friction. However, the touching mode may cause some defectives, such as deformations and damages on the samples.

In tapping mode of AFM, the imaging mechanism is similar to that of contact AFM with a resonant frequency of oscillating the cantilever. The constant oscillation of the tips from the sample-probe interaction can image biological samples. It makes challenges in the liquids sample. Also, low scanning speed is better to keep during measurements.

In non-contact mode of AFM, there is no contact between the sample surface and cantilever but oscillating above the adsorbed fluid layer during scanning. The changes in amplitudes of oscillation due to the attractive VDW's force interaction measure the surface topography of samples. The disadvantages including low resolution and also the ultrahigh vacuum condition is needed in case the contamination layer on the sample might oscillate with the cantilever [114].



The real experimental AFM machine is shown in Figure 2-10.



Figure 2-10. Atomic force microscopy

2.2.3. Transmission electron microscopy (TEM)

TEM is the microscopic technique which can analyze the structure of specimens in high resolution even down to an atomic precision. The characterization of specimens including the morphology of sample, defects, crystal structures, phase and compositions, and the magnetic micro-structure can be performed. The functions of TEM involve electron-optical imaging, electron diffraction and small probe capabilities. Moreover, experiments can investigate the structural information of the target materials in situ by alterations of environmental factors in TEM. It implies that accommodation of samples in TEM has size restriction for the electron transmission. Also, TEM has the illumination system to transfer the electron beams to the specimen by either focused or broad beams.

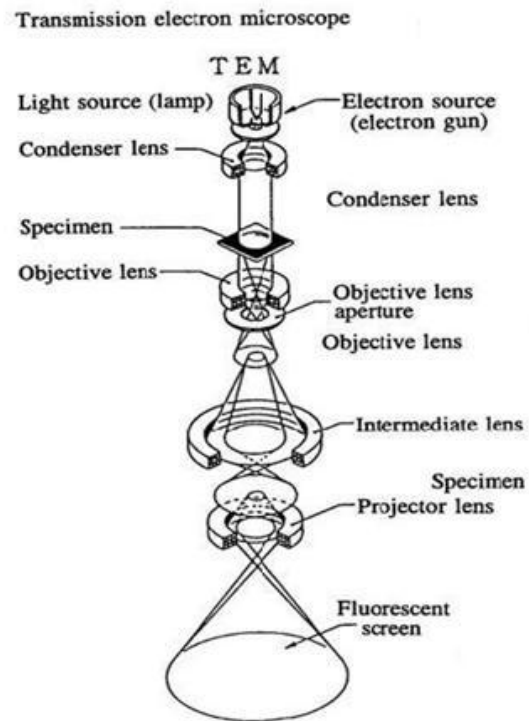
A high energetic electron beam transmitted through the samples so as to image and analyze the crystal structures in an atomic scale resolution. Electron beam is focused by passing through the electromagnetic lens and accelerated under several hundreds kV applied which is shown in Figure 2-11. Application of



THE HONG KONG POLYTECHNIC UNIVERSITY

electric field can varied the wavelength smaller than that of light. For example, 200 kV electron beam can give a wavelength at 0.0025 nm. After that the beam is magnified and focused onto imaging devices such as intermediate or projector lens. The image on the fluorescence screen is able to record by digital camera. In general, the optical microscopy is limited by the wavelength of light sources. However, the resolution of TEM image is restricted by intrinsic aberrations in electromagnetic lens (~0.1-0.2 nm).

The high resolution mode of TEM can image the crystal lattices of materials by interference pattern of transmitted and reflected beams in atomic scale resolution. Hence it is able to observe the planar and line defects, grain boundaries and the interfaces from cross section. There are two fundamental modes, including bright-field or dark-field mode allowed (100) transmitted beam and excluded (100) beam, respectively. The size of objective aperture is tuned for eliminating all diffraction beams to obtain low resolution defects which are called diffraction contrast. The orientation of crystal structure of specimens can be excited by the diffracted beams in a particular direction in order to distinguish the thickness of specimens, the defects and crystal lattices affected by strains and bends [115]. Figure 2-12 shows the instrumentation setup of TEM.



[115]

Figure 2-11. Working principle of TEM



Figure 2-12. TEM system



2.3. Optical measurement techniques

2.3.1. Raman spectroscopy

Raman spectroscopy is used for the vibrational or rotational bonds testing of the specimens by irradiating the monochromatic light on specimens. When the light is incident into those materials, the excitations of bonds vibrating and rotating between the molecules will scatter the light. It composes various wavelengths differed from the incident one and will be collected by Raman spectroscopy. When the specimen is illuminated, molecules from those samples will absorb energies and jump to the upper energy states. After that, the photons will be emitted immediately because of the instability and fall back to lower energy level. Figure 2-13 shows three conditions about excitation of molecules to upper vibrational levels. The condition **a** described by the wavelength of incident light is equal to that of the scattered light, which is called Rayleigh scattering. The condition **b** shows the molecules fall back to a vibrational level higher than the original so that longer wavelength of scattered light will be emitted. It is called stokes limit scattering. The situation **c** totally reverses from the condition **b** in which the excited molecules fall down to the vibrational level lower than the original so that shorter wavelength of scattered light will be emitted. It is called anti-stokes Raman scattering [116].

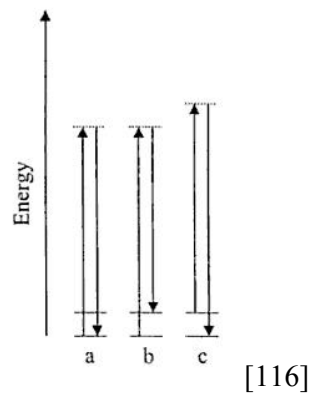


Figure 2-13. Schematic diagram of Raman scattering

When a majority of molecules in the specimen are illuminated, the collection of intensity of Stokes Raman scattering is also high. The intensity of anti-Stokes Raman scattering is proportional to number of molecules excited in the next upper vibrational level. As Boltzmann distribution equation described, there is large number of molecules in lower vibrational energy level than that in higher vibrational level at equilibrium condition. It implies that Stokes Raman scattering has higher intensity than that of anti-Stokes Raman scattering so that the degree of intense anti-Stokes Raman scattering can be neglected. Raman spectroscopy is a technique to measure the shift between the incident and Stokes Raman scattered light which is called Raman shift shown in Equation (3).

$$\text{Raman shift} = \frac{1}{\lambda_{\text{incident}}} - \frac{1}{\lambda_{\text{Raman scattering}}} \quad (3)$$

Raman shift can find out the particular energy of vibrational bonds in the specimens, representing the corresponding bonding so that whatever the bonds composes of specimens can be realized [116].

In this project, Raman spectroscopy is used to investigate the identification and number of layers of WS₂. The wavelength of solid-state laser used in

experiment is 488 nm and the numerical aperture (NA) objective lens is used ~ 0.9 . The Raman spectroscopy used is shown in Figure 2-14.

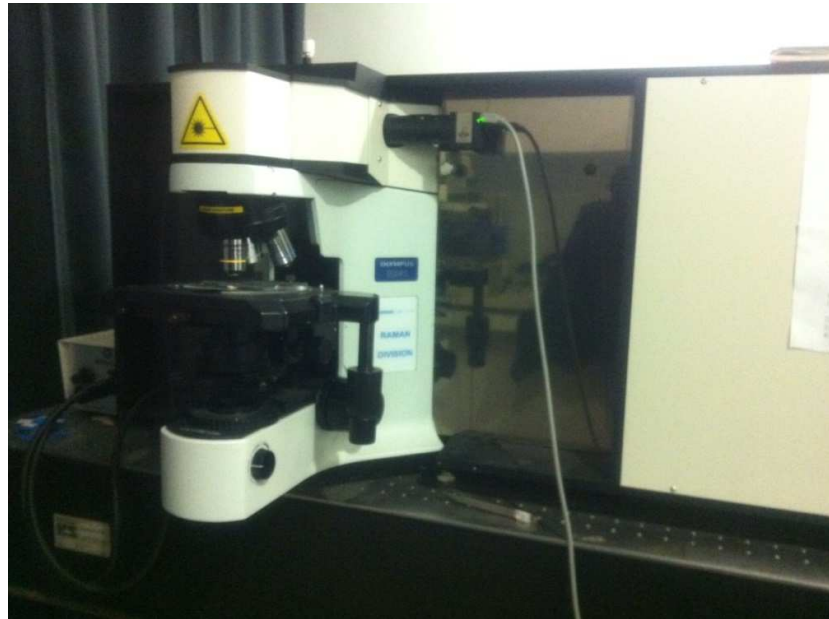


Figure 2-14. Raman spectroscopy

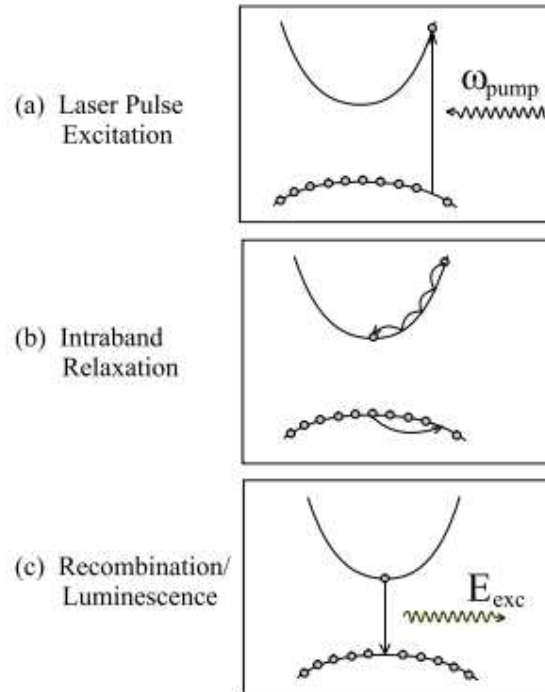
2.3.2. Photoluminescence spectroscopy

Absorption, PL and photoluminescence excitation (PLE) measurements are the spectroscopic methods generally used to characterize the optical transitions in semiconductors.

The theory of photoluminescence measurements can be described by three stages shown in Figure 2-15. First of all, the use of femtosecond laser pulse with energy equal to $\hbar\omega_{pump}$ is needed to excite the electrons of the specimen from fully occupied valence band to the empty conduction band and electron-hole pairs will be generated. After that those electrons and holes in non-equilibrium condition will undergo relaxation and incline to fall back to ground state. The

intra-band relaxation is formed due to the transfer of energy to the crystal lattice as step-by-step excitation of lattice vibrations, for example, primarily longitudinal optical phonons in polar semiconductors at low temperatures. Finally, the electron-hole pairs recombine together by light emission known as PL process. The existence of coulomb interactive attraction among the charge carriers leading to inclusion of emission spectrum from energy states at or above fundamental band gap. Thus the discrete lines just below band gap energy come from the bound excitation energy states [117].

In this project, we will compare the photoluminescence spectra of Au/WS₂ flakes to demonstrate the PL enhancement induced by LSPR. PL spectroscopy is measured from the same system of Raman spectroscopy.



[117]

Figure 2-15. Three mechanisms including laser pulse excitation, intra-band relaxation and recombination.



2.3.3. Ultra-violet (UV) visible spectroscopy

The most conveniently available and familiar source responsible for the visible spectroscopy is the tungsten lamp. When the power supply is started up, the given current causes lamp filament to brighten and emit an intense white light accompanied with a considerable amount of heat. Radiation from the filament constitutes various wavelengths. However, the emitted particular wavelength is highly dependent on the temperature of the source known as 'black body radiation'. Also, deuterium lamp is responsible for UV region. Two sources are composed of entire UV-visible wavelength.

UV or visible light will be absorbed by many kinds of materials. The absorbance of materials can be counted in the degree of attenuation of incident beam source. Beer's law states the relationship of absorbance (A), path length (b) and concentration (c) of the target species:

$$A = ebc \quad (3)$$

where e is a constant of proportionality.

An absorption spectrum will give a numerical absorption bands corresponding to the structure in the species.

Atoms or molecules exists in materials involve numerical energy states. When the radiation regarding as large amount of photons incident into species, integral number of the photons will be absorbed or emitted to transit from those energy levels. The internal energy of molecules in substances is equal to the sum of energies of their electrons, also the vibrational energy between constitution atoms and the rotational energy of molecules. Usually vibrational and rotational energy level packed on the top of each electronic level. Either absorption of UV

or visible radiation is due to the excitation of outer electrons from molecules. There are three types of electronic transitions, such as transitions involving p, s and n electrons, transitions involving charge-transfer electrons and transitions involving d and f electrons [118, 119]. The UV-visible spectroscopy used during the experiments is shown in Figure 2-16.



Figure 2-16. UV-visible spectroscopy

2.4. Summary

To summarize, in this project we will adopt the sulfurization of thin tungsten film in which the thin tungsten film was sputtered on the SiO_2/Si substrate placed into the tube furnace for the reaction. After fabrication of WS_2 , SEM, AFM and TEM characterization will be done for testing the morphologies of this 2D material. Furthermore, the Raman spectroscopy has been followed to chase the identity of as-prepared material. After confirmation of 2D WS_2 , the optical properties can be tested by PL and absorption spectroscopies to do characterizations in advances.

Chapter 3. Fabrication and Characterizations of 2D WS₂ and AuNPs

This chapter provides overview of experimental conditions in fabrication of 2D WS₂ crystals and the synthesis of gold nanostructures. Besides the descriptions of experimental procedures, the characterizations of WS₂ and gold nanostructures, including structural information and measurements of optical properties, are given in details. It will be divided into few sections, including experimental conditions and procedures of sulfurization of thin tungsten film, seed-method synthesis in gold nanostructures and the characterizations of as-prepared WS₂ crystals and synthesized AuNPs, and the experimental procedures for fabrication of hybrid AuNPs/WS₂ nanostructures.

3.1. Fabrication of 2D WS₂

3.1.1. Sulfurization of transition metal film

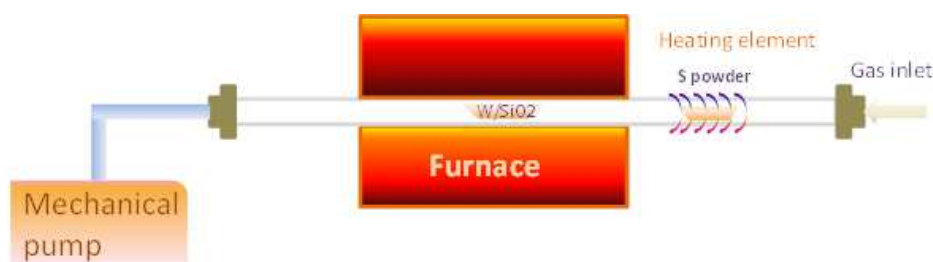


Figure 3-1. Schematic diagram of setup using for the sulfurization of TMDs materials

In the fabrication process, the sulfurization of transition metal film was adopted to fabricate the monolayer WS₂ by the equipment shown in Figure 3-1.

First, sputtered tungsten film with below 10 nm thick was grown on 1 μm Si/SiO₂ substrate. The sputtering rate of tungsten material was characterized by estimating three points of thicknesses with different time intervals on the same target-to-sample distance, chamber pressure and power.

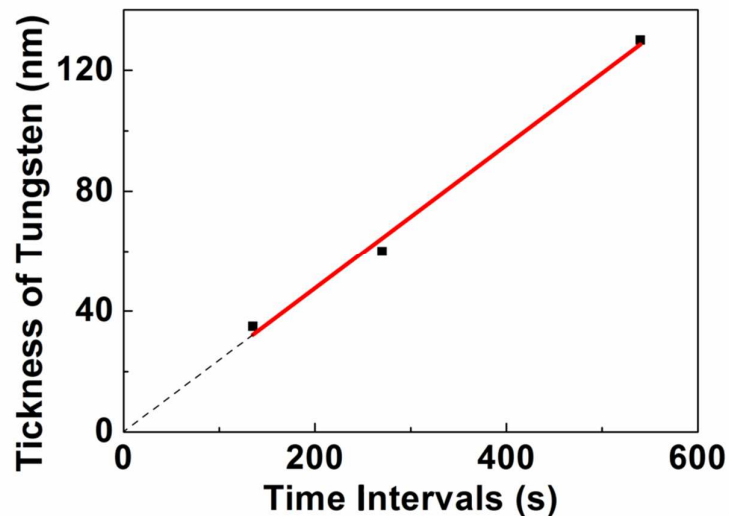


Figure 3-2. The calibration of deposition rate of tungsten material obtained from magnetron sputtering.

From Figure 3-2 shown above, the sputtering rate of the tungsten material with same sputtering conditions is about 2.3 $\text{\AA}/\text{s}$. According to the previously reported results [44, 45], about 5 to 10 nm sputtered tungsten film was deposited on the substrate. Afterwards, these substrates were placed on the ceramic boats and these boats were put into the quartz tube. Purging Argon gas in 15 minutes before launches the furnace in order to remove all impurities inside. Then, the pressure was controlled in 300 Pa and ramping temperature to 750°C gradually.

Before reaching the target temperature, the filament was switched and hold for 10 minutes. Finally, it was cooled down to room temperature.

3.1.2. Results and characterization

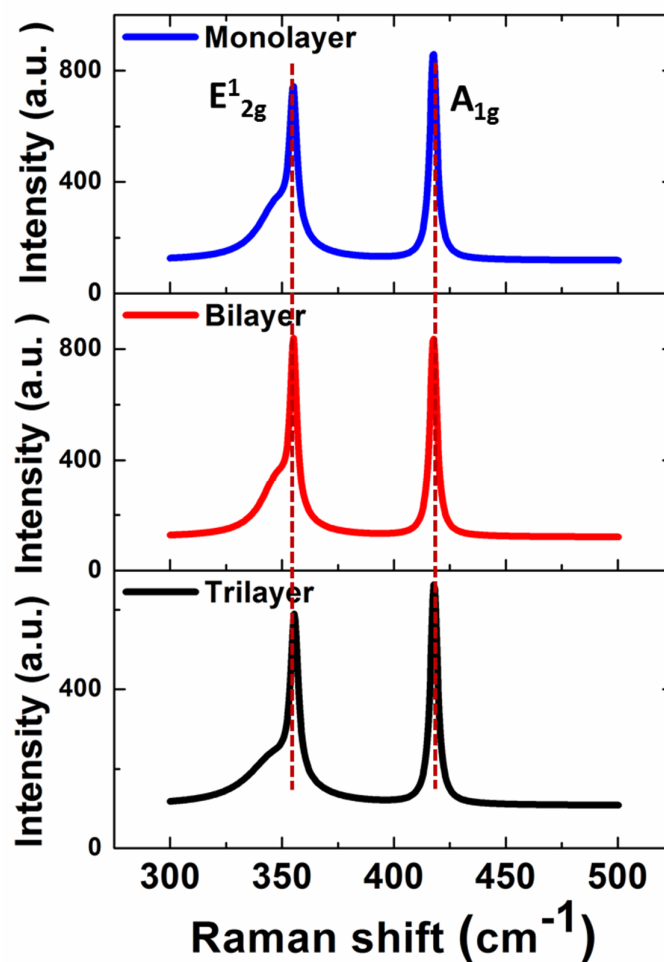


Figure 3-3. Raman spectra with respect to the monolayer, bilayer and trilayer WS_2 .

There are many descriptions of Raman spectra about multi-layered WS_2 from the previous reports [52]. In these spectra, the longitudinal acoustic mode at M point can be distinguished the first-order modes including $E^1_{2g}(\Gamma)$ and $A^1_g(\Gamma)$



at the Brillouin zone center and the disorder activating zone edge mode. The in-plane phonon mode LA (M) of the longitudinal acoustic mode in a lattice is a collective movement from atoms like a sound wave. The lattice will experience a periodic compressions and expansions along the propagation direction. The symbol M in the M point of the Brillouin zone refers to the particular direction and the momentum of the phonon in the dispersion relation between frequency and momentum. From the exfoliation and chemically fabricated WS₂, the first-order optical modes E¹_{2g} (Γ) and A_{1g} (Γ) will be analyzed especially. From Figure 3-3, the 488 nm excitation wavelength has been used. From bulk to monolayer, the absolute intensity of Raman modes will decrease gradually due to the occurrence of optical interference between the excitation energy and Raman signals emission. In monolayer, the E¹_{2g} (Γ) and A_{1g} (Γ) modes are 354 cm⁻¹ and 417 cm⁻¹. It has been described that thickness will respond to Raman modes. When the number of layers increase, A_{1g} (Γ) mode will give a blue shift and in vice versus, 2LA (M) and E¹_{2g} (Γ) will give a redshift. The blue shifting of A_{1g} (Γ) increasing the stiffness of WS₂ is due to the VDW's forces among the layered structures. Also, the thicker WS₂ with redshift in Raman mode E¹_{2g} (Γ) shows an anomalous dielectric screening change due to the long range Columbic interaction between the effective charges. From mono-layer to tri-layer WS₂, the value of Δk corresponds to 61.6 cm⁻¹, 63.6 cm⁻¹ and 64.5 cm⁻¹ [32].

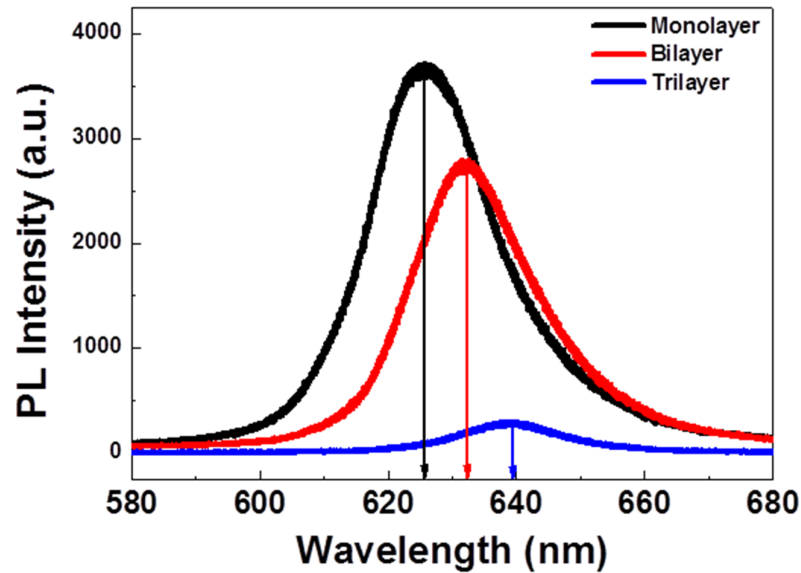


Figure 3-4. The corresponding PL spectra related to the monolayer, bilayer and trilayer WS_2 in Figure 3-3.

The monolayer triangle WS_2 has a strong PL emission because of its direct band. When the layers increase from monolayer to trilayer, the PL intensities gradually decay due to the bandgap shift from direct to indirect transitions [51, 52]. From Figure 3-4, the peak wavelength from monolayer to tri-layer increase is changed from 626 nm, 633 nm to 640 nm, indicating the red-shifted PL depending on the thickness of WS_2 .

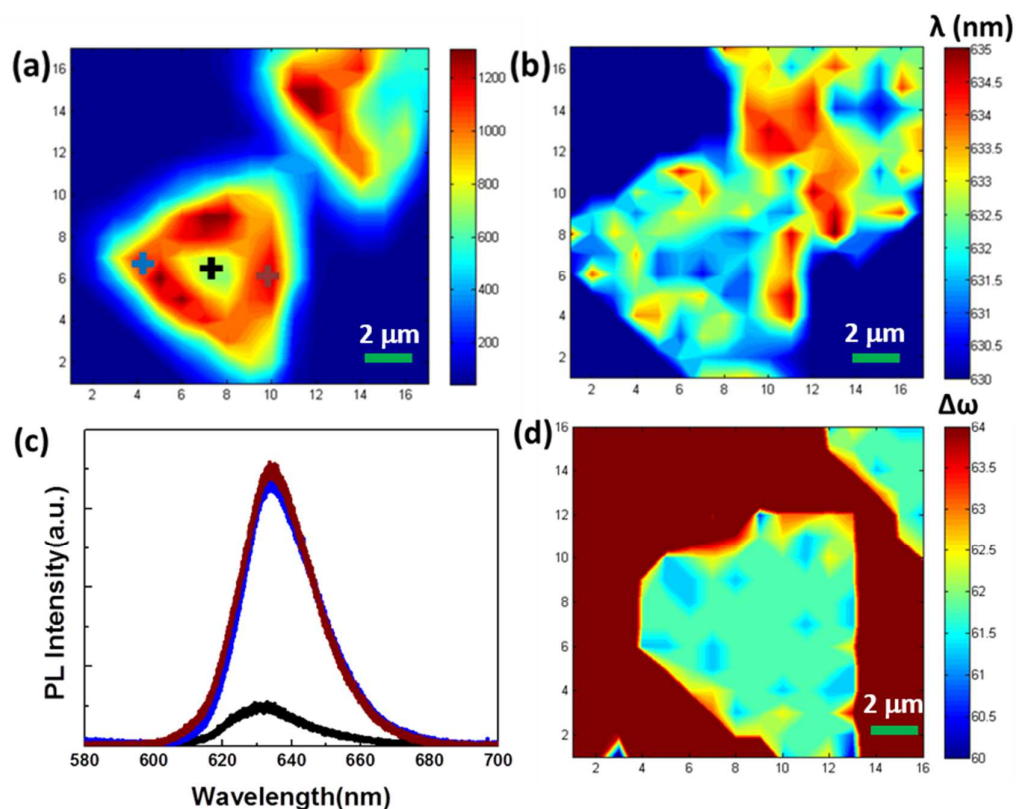


Figure 3-5. (a) Spatial distribution of photoluminescence intensity with scanning the whole WS₂ flake. (b) Spatial distribution of peak intensity's wavelength with scanning the whole WS₂. (c) PL spectra with corresponding color points in Figure (a). (d) Spatial distribution of Raman shift $\Delta\omega = A_{1g} - E^1_{2g}$ with scanning the whole WS₂. All of the spectra are in μm along both x - and y -axis.

The light emission of monolayer WS₂ can be described in detail by conducting micro-photoluminescence mapping. It shows the peak positions, widths and intensities of PL varied from the edges to centers of triangle in Figure 3-5. Figure 3-5 (a) shows the strong light intensity emitted from the edge, however, the emission quenches when gradually moving towards to the triangle center and recovers gradually at the edge of triangle. From Figure 3-5 (b), it reveals the corresponding spatial distribution of peak's emission wavelength in the same WS₂,

which is evident that longer emission wavelength prefers at the edge relative to that of center. The fact of the central part of triangle WS_2 has emitted blue-shifted wavelength rather than that around WS_2 edges. Figure 3-5 (c) shows full PL spectra extracted from Figure 3-5 (a), ranging from the edge to the body centers of WS_2 . Figure 3-5 (d) shows the spatial mapping of the angular frequency from two active Raman modes (Γ) E_{2g} and A_{1g} is near 61.7 cm^{-1} to verify the monolayer of triangle WS_2 by Raman spectroscopy using a 488 nm solid-state laser.

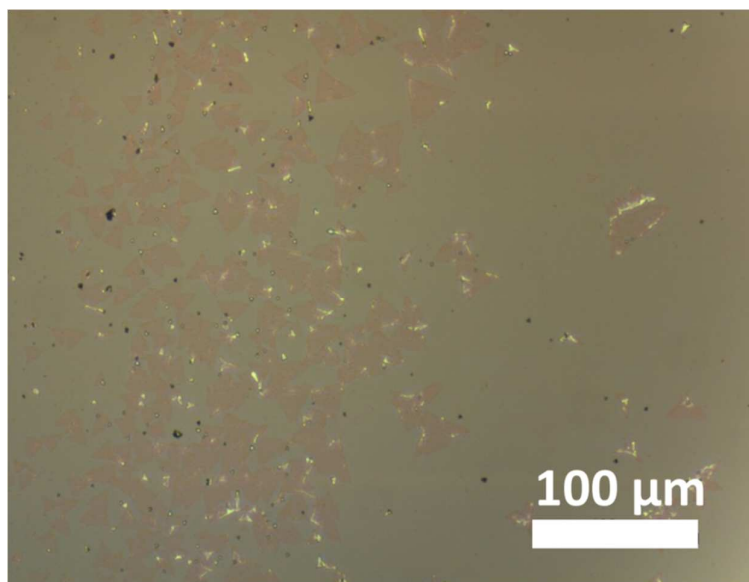


Figure 3-6. Optical microscopy from WS_2 sample fabricated by the sulfurization of thin tungsten film.

The optical microscopy and scanning electron microscopy (SEM) images taken from the as-prepared WS_2 show a wide sized-distribution roughly from 10 μm to 40 μm with random overlapping triangle WS_2 morphology.

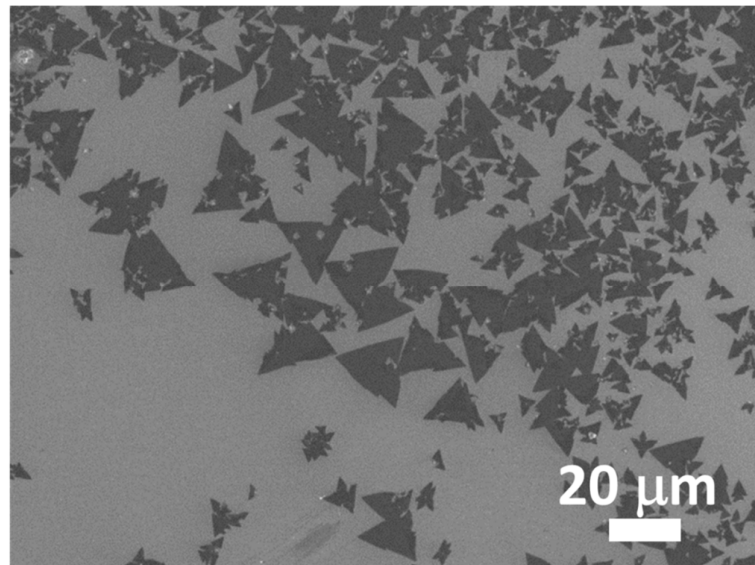


Figure 3-7. SEM image from WS₂ sample fabricated by sulfurization of thin tungsten film.

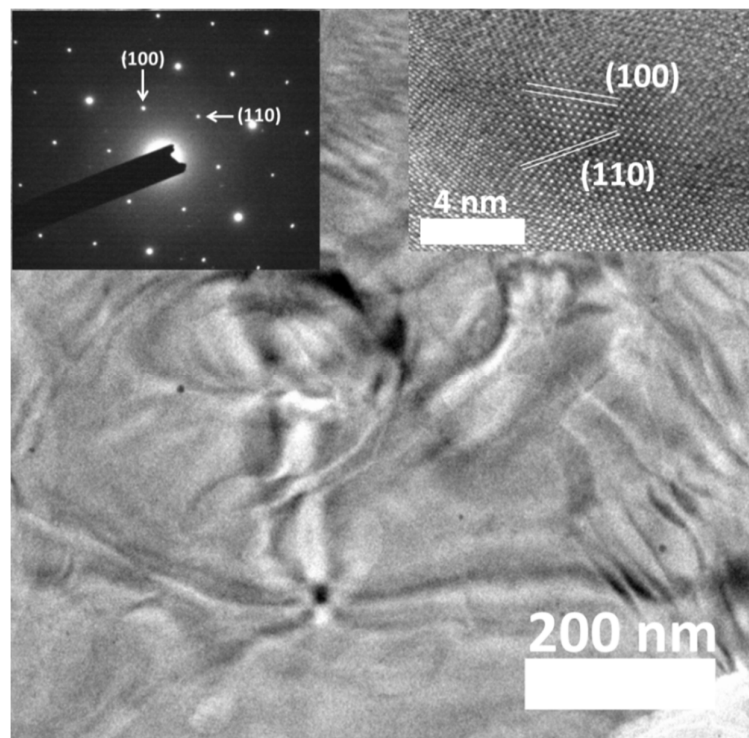


Figure 3-8. TEM image from WS₂ sample. The left inset shows the selected electron area diffraction (SEAD) and the right inset shows the corresponding HRTEM image.

Figure 3-8 represents the transmission electron microscopy (TEM) details in WS₂ monolayer. The morphology of larger area of WS₂ can be visualized. The right inset is the HR-TEM images of WS₂ with labeled (110) and (100) miller index notation. It shows the sharp edges are at the micro-scale perpendicular to the [100] crystallographic direction. Figure 3-9 shows the measurement of ratio of elemental composition of tungsten and sulfur equal to 1:2 measured by EDS.

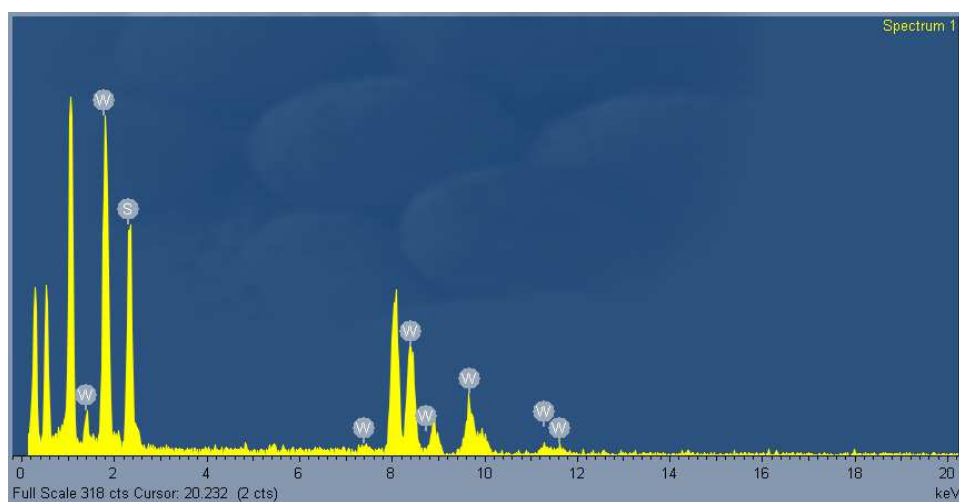


Figure 3-9. The EDS image

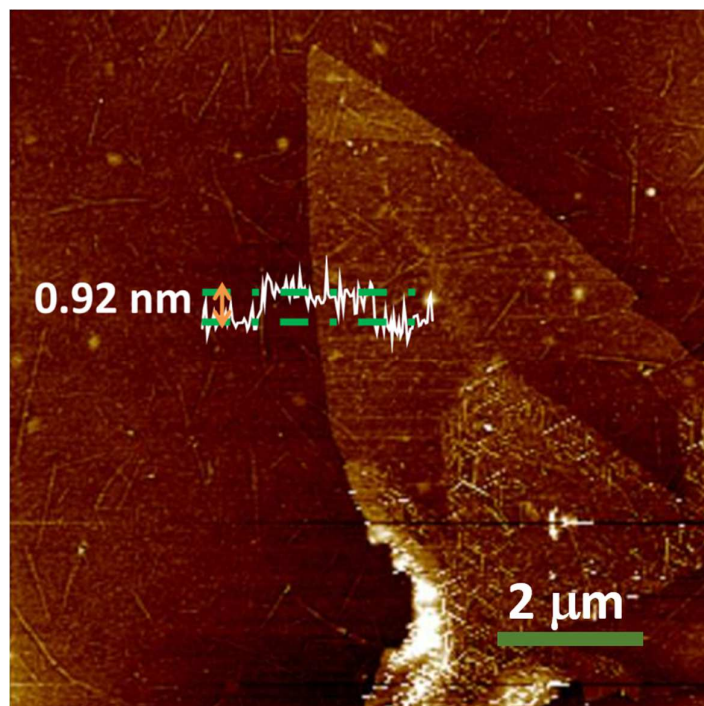


Figure 3-10. AFM images from as-prepared WS₂ sample.

Figure 3-10 shows the height profile. It is clearly seen that the thickness of monolayer WS₂ is about 0.92 nm by the AFM.

3.2. Synthesis of gold nanostructures

3.2.1. Seed method synthesis of AuNRs

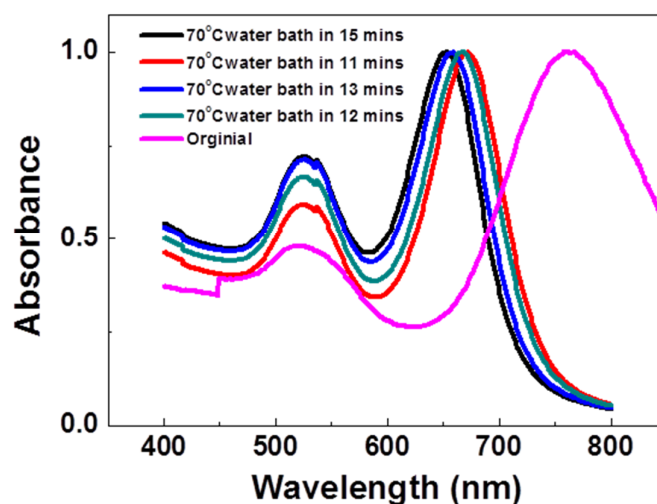
Gold nanorods (NRs) can be synthesized by using seed-mediated method. In brief, the first step is to prepare the Au spherical NPs as the seed solution. After that, 0.25 mL of an 0.01 M aqueous solution of HAuCl₄•3H₂O mixed with 7.5 mL of 0.1 M cetyltrimethylammonium bromide (CTAB) solution as the stabilizer to hold the shape of the AuNPs. Remember to mix by the up-to-down inversion. Then 0.6 mL of 0.01M ice-cold NaBH₄ solution added at once and let a rapid



mixing inversion to ensure the whole process completed in 2 minutes. Then stored it at room temperature and used after two hours preparation.

In the second step, in order to prepare gold Nano rods, 0.6 mL of 0.01 M $\text{HAuCl}_4 \cdot 3\text{H}_2\text{O}$ and 0.09 mL of 0.01 M AgNO_3 were added into 14.25 mL of 0.1 M CTAB and made by slightly inversion mixing. 0.096 mL of 0.1 M ascorbic acid solution was then added. The solution B was well prepared. Finally, 0.063 mL of the seed solution was added into solution B and mixed for 10s. The growth of AuNRs can be produced in this methodology. However, through the mild oxidation in different time period, those AuNRs can be exhibited a size reduction. How fast the size reduction undergone is dependent on the temperature and acidic concentration. A few drop of as-prepared 1M of Hydrochloric acid was added into the as-synthesized solution before immersing it into water bath at 70°C. After 15 minutes later, the selective aspect ratio AuNRs with absorption peak at 655 nm can be synthesized [120].

3.2.2. Results and characterization





THE HONG KONG POLYTECHNIC UNIVERSITY

Figure 3-11. Absorption spectra of the oxidative gold nanorods during different time intervals.

The absorption spectrum with peak wavelength at 770 nm can be obtained from measurement of the as-prepared AuNRs following the original receipt reported previously. However, when the mild oxidation conducted with different interval in acidic medium, it may induce a variation on average aspect ratio of AuNRs and the corresponding absorption spectra as well. Figure 3-11 shows the combined absorption spectra with different stages of AuNRs oxidation. Shortening the length of AuNRs by oxidation arises a blue shift resonance in the absorption spectrum with varied longitudinal plasmon wavelengths (LPW) exhibiting a distinct color from the particle solution. In the normalized absorption spectra, it shows the highest peak at ~650 nm and the second weakened peak at 525 nm corresponding to the transverse plasmon band (TPB) and longitudinal plasmon band (LPB) [121]. The portion of LPB emerges blue-shift peak positions but keeping constant in the peak intensities during oxidation occurs. The longitudinal plasmon resonance peaks with full-width-half-maximum ranging from 70 nm to 150 nm. The shorter wavelength peaks at 525 nm remain unchanged. At the same time, the TPB show no change in peak positions but enhanced peak intensities indicate the conversion of AuNRs into nanospheres partially. However, the portion of those spherical AuNPs is over half of the as-prepared solution in the normalized absorption spectrum in Figure 3-12. The portion of AuNRs has been increased to ensure the majority of AuNRs coating on 2D materials. The abundance of Au spheres can be suppressed by using the ice-cold NaBH₄ solution instead of room temperature NaBH₄ so the efficiency of

producing AuNRs can be enhanced as below.

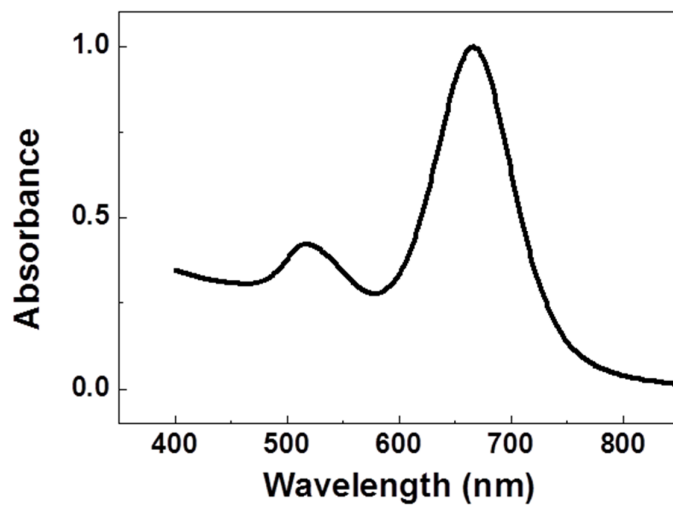


Figure 3-12. The absorption spectrum from the gold nanorods with optimized aspect ratio.

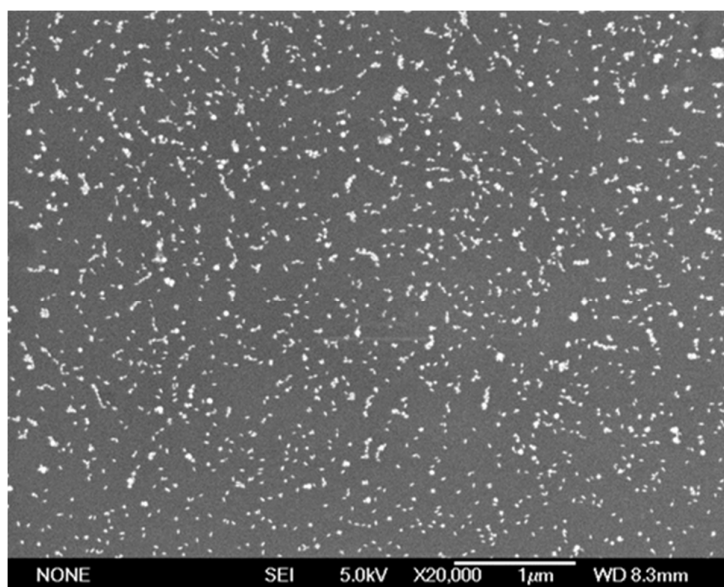


Figure 3-13. The corresponding SEM image from the same experimental condition in Figure 3-12.

The AuNRs can be retrieved from the mixture including surfactant and nanospheres from seed solution by centrifuge. Extracting 10 mL synthesized solution centrifuges at 6000 rpm for 30 minutes. After centrifuge the supernatant including less weight of constituents such as gold nanospheres and CTAB surfactant can be removed so that a majority of AuNRs were disperse in 0.1 mL DI water. Those reminders were dropped on the Si substrate to capture the morphology from SEM image in Figure 3-13. However, due to the resolution limitation of SEM images, it is only possible to observe the aggregation of AuNRs rather than less dispersive AuNRs in the majority. Figure 3-14 shows the dispersion of AuNRs in the TEM image with the low-magnification in which the morphology of AuNRs can be observed clearly. And the corresponding HRTEM image of AuNRs with aspect ratio at 2.2 in Figure 3-15. The average distribution of AuNRs with aspect ratio was retrieved from the LMTEM image in Figure 3-16. It shows the predominant aspect ratio from those synthesized AuNRs at around 2.8.

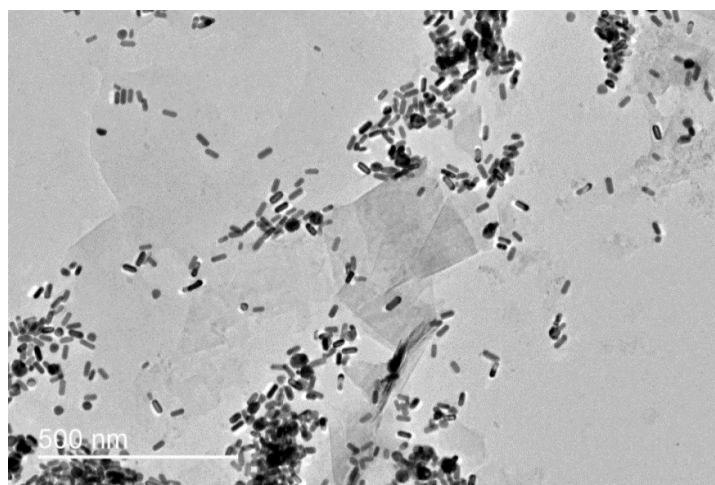


Figure 3-14. LMTEM image of nanorods growth.

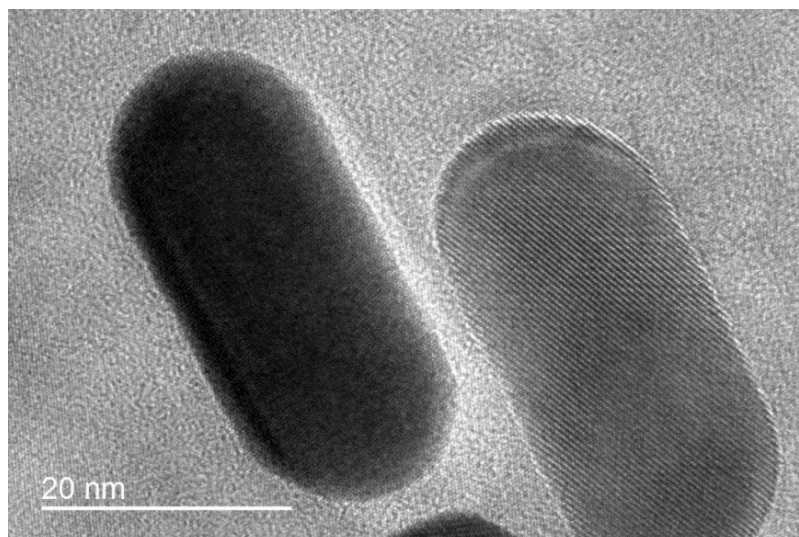


Figure 3-15. HRTEM image showing the mean aspect ratio of AuNRs is around 2.2.

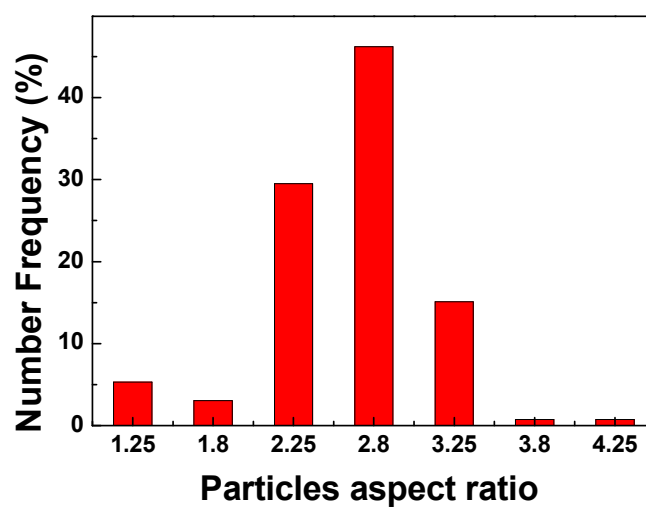


Figure 3-16. The prominent AuNRs aspect ratio extracted in Figure 3-14 is around 2.8.



3.3. Experimental procedures for hybrid Au/WS₂ structures

3.3.1. The formation on AuNPs/WS₂ by HAuCl₄ chemical solution

The as-prepared WS₂ sample was immersed into the aqueous solution of HAuCl₄ with different concentrations. The DI water as the solvent to coat the AuNPs onto the sample and it is one of the less-defective methods for the preparation of AuNPs/WS₂ nanostructure. After the confirmation of successfully fabricated WS₂ micro-sized flakes, the as-prepared WS₂ samples were immersed into 5 mM HAuCl₄ aqueous solution in time intervals of 40 s at room temperature. After that, WS₂ was put into a dry box and dried for 4 hours [101]. However, it is difficult from the sample to stay away totally from the moisture completely.

3.3.2. The preparation of AuNRs/bilayer WS₂ hybrid nanostructure

The synthesized AuNRs were dropped on the WS₂ samples after centrifuge process to get rid of the surfactant CTAB as much as possible. After drying the reminding solution on the WS₂, it is needed for the sample to immerse into the DI water once in order to re-dissolve any CTAB residues on the sample. However, from the experimental results, it suggests that it is one of defective methods for fabrication of the AuNRs/WS₂ nanostructure due to the presence of surfactant CTAB causing damages such as some stretching or removal on the integrated morphologies of WS₂. Therefore, the experiments must be repeated until the integration of WS₂ produced.

3.3.3. Thermal evaporation of gold nanoparticles on WS₂ substrate

5 mg weight Au wires was used to deposit a thin film on the sample by the



thermal evaporator. Before the film deposition, the chamber is needed to keep pressure down to 7.5×10^{-5} mTorr. It takes two minutes for the Au deposition process and one hour is needed for cooling down. After taking out the sample from chamber, Au islands have been deposited and afterwards annealing has been undergone when placing into the tube furnace without any gases flowing. The sample was pumped down and annealed at 600°C. During the heating process, the Au islands will gain the thermal energy so as to aggregate to form AuNPs. The less weight of gold wires and high temperature annealing will help to form Au nanosphere with diameters less than 50 nm.

3.4. Summary

To summarize, the few layers of WS₂ have been successfully fabricated by sulfurization of thin tungsten film introduced in Chapter 2. Through various techniques, structural and optical analyses are performed. According to demonstration of structural information, optical images and SEM measurements indicate the morphologies of WS₂ with the size distribution at around ~ 20 μm . At the same time, the identity and thickness measurements have been taken by Raman spectra, height resolution TEM images and AFM image with corresponding height profile. After that, the optical properties are analyzed by PL spectra and absorption spectra. After successful fabrication of WS₂, the as-prepared AuNRs have been synthesized and undergone characterization. And finally those as-prepared AuNRs will be coated onto the WS₂ to form the hybrid Au/WS₂ nanostructure which will be shown in Chapter 4.





Chapter 4. Optical and PL Properties of WS₂ Decorated with Gold Nanoparticles

A few reports have referred to the PL enhancement from TMDs materials via plasmonic effect. The earlier study [73] suggested that exciton-plasmon interaction could be established between plasmonic resonator and 2D WS₂ in order to enhance light emission. In this work, AuNPs are decorated on the WS₂ via a simple chemical method. The spatial distributions of nano-sized Au on 2D WS₂ have been observed through electron microscopy characterization. The PL measurement has been performed for the WS₂ sample with and without AuNPs coating. From the literature reviews [67, 68], the enhancement of PL emission is mainly attributed to the intensity enhancement by the LSPR of the AuNPs. Particularly, those enhanced excitonic emission after the decoration of WS₂ is a signature of the enhanced PL, which is amplified by the field enhancement arising from LSPR excitation.

The MNPs are able to be either a radiative quencher or a radiative enhancer, critically depending on the compositions, sizes, geometries and distances between organic molecule donors and MNPs. If the donor molecules were placed in the proximity of MNPs, not only the resonant energy transfer but also the radiative lifetime of donor molecules would change. The quenching effect might occur within the small interspacing from the metallic quenchers resulting in the reduction of PL. Therefore, the most sophisticated relationship between the degree of electric field at surface of MNPs and the dielectric dispersion manipulating in the possible situations in either quenching or enhancement must be not neglected.

Also, the special design of the AuNP is needed for PL enhancement.

4.1. PL enhancement via various AuNPs decorations methods

4.1.1. Au/WS₂ nanostructure from HAuCl₄⁻ immersion

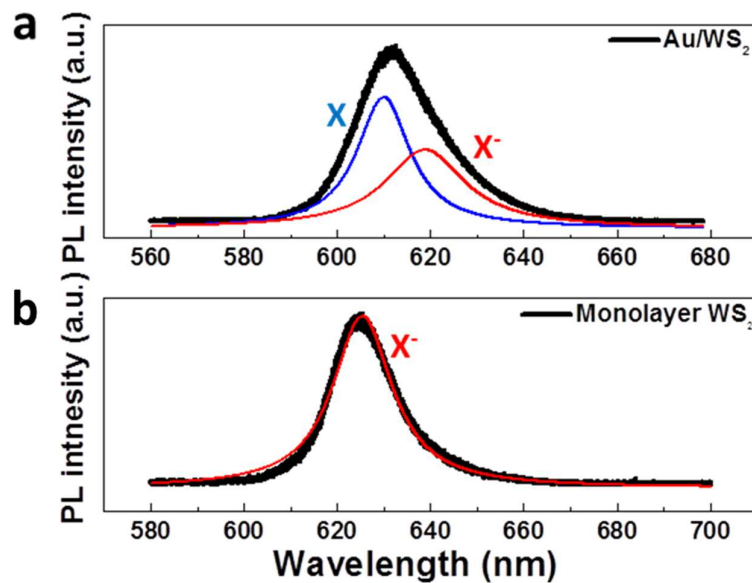


Figure 4-1. PL spectra with exciton/trion emission (labeled by X/X⁻ respectively) from (a) bare WS₂ sample and (b) Au/WS₂ sample by Lorentzian fit in monolayer WS₂.

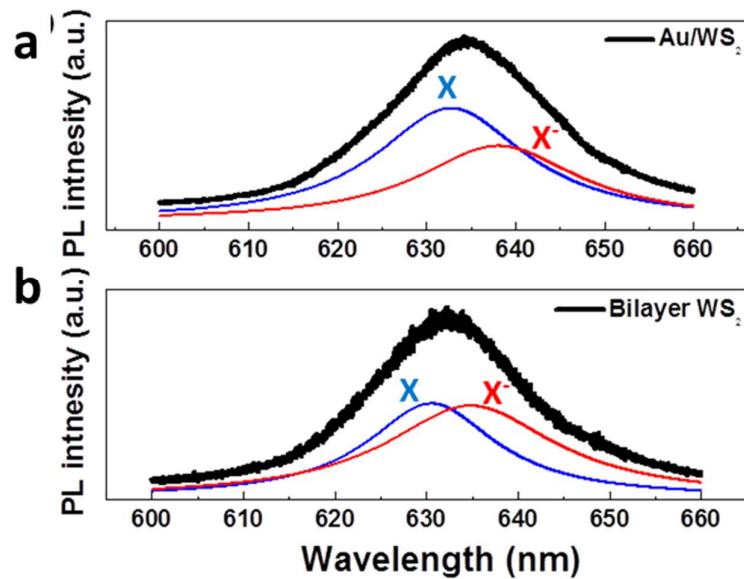


Figure 4-2. PL spectra with exciton/trion emission (labeled by X/X⁻ respectively) from (a) bare WS₂ sample and (b) Au/WS₂ sample by Lorentzian fit in bilayer WS₂.

In Au/WS₂ hybrid nanostructure, it is possible to raise the excitons and trions emissions analogue to the chemical doping in MoS₂/WS₂. Figure 4-1 (a) shows the trions (X⁻) emission called electron-bound exciton emission at ~1.98 eV from PL spectrum with the measurement of WS₂ at room temperature coincided with previous reports [122, 123]. It was attributed by full trion recombination due to the unintentionally n-type doping on bare WS₂ materials [104]. Two PL features in optical responses by Lorentzian fits are at ~2.04 eV and ~2.00 eV respectively. The higher energy peak contributed for emissions of neutral excitons (X). The model of exciton/trion formations can be interpreted as followed: when light illuminated onto WS₂, it will be emitted into two parts, one is the photo-generated X and the other is the formation of X⁻ from a partial photo-generated X. When p-type doping occurs, the depletion of excess electrons would be



aggravated and the predomination of electron-hole recombination turned from X^- to X. After decoration of AuNPs, the binding energy of monolayer WS_2 increases from ~ 14 meV to 22 meV. However, the formation of X would contribute to a substantial proportion of light emissions as the result of large exciton effect comparing to the trions binding energy of Au/monolayer WS_2 (~ 40 meV) [124] and typical two-dimensional semiconducting materials (1-6 meV) [105, 125]. However, the reason on the PL enhancement of monolayer WS_2 is possibly due to preparation of aqueous $HAuCl_4$ solution by deionized water as the solvent. The withdrawal of charges results from the adsorption of H_2O molecules to the monolayer WS_2 crystals. It is incapable of attributing the varied PL emissions completely from the LSPR effect. However, the same process conducted by adoption of the bilayer WS_2 makes less effective for the charge transfers resulting in variation of trions/excitons emissions in Figure 4-1 and Figure 4-2.

Figure 4-2 shows the optical response of bilayer WS_2 predominated by both X and X^- features due to weaken the n-type substrate doping. By comparing the light emissions of bilayer to monolayer, bilayer shows weaker exciton effect. The electrons from the conduction band was transferred to AuNPs to suppress the X^- formation which is proportional to the charge carrier density on WS_2 [104]. The suppressed X^- formation also leads to the PL quenching.

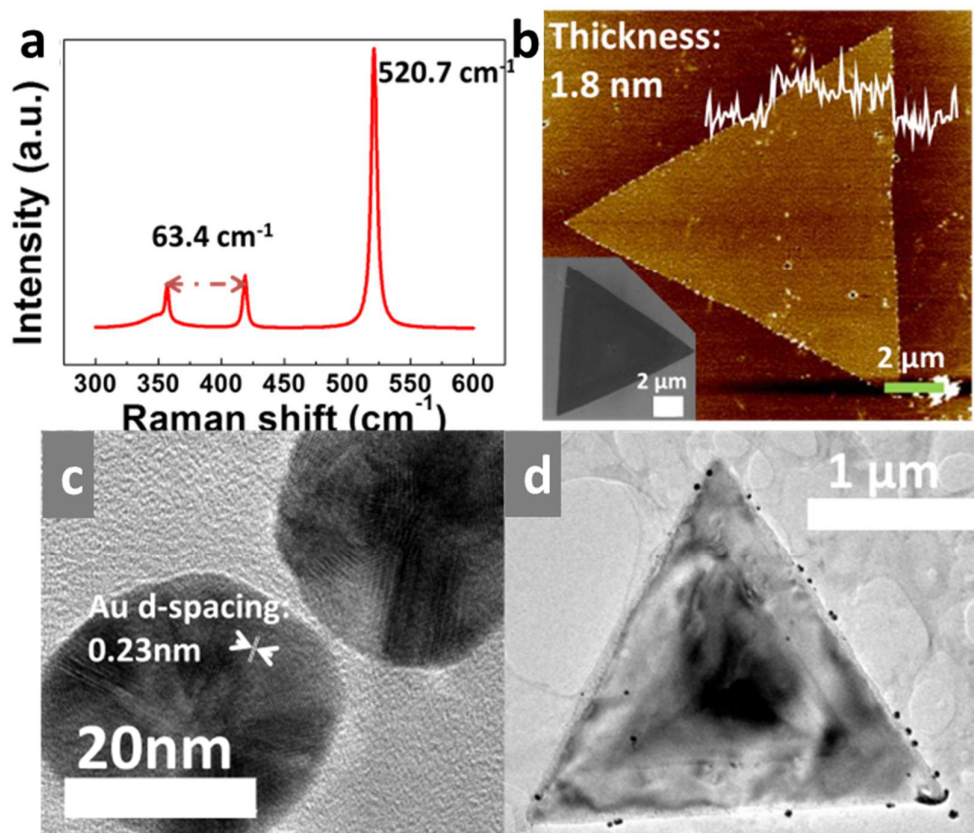


Figure 4-3. Structural characterization of the synthesized nano-composites of 2D WS_2 crystals and AuNPs. (a) The Raman spectrum of a bilayer WS_2 characterized with Si substrate at 520.7 cm^{-1} . (b) The corresponding AFM image with the height profile was measured and the inset shows the SEM images with same WS_2 flake. (c) Enlarged TEM image shows the spherical AuNPs adhered onto the edge of WS_2 . (d) Low magnification TEM image with the triangular Au- WS_2 flake.

A strong evidence is given the number of layers of WS_2 flakes characterized by Raman spectroscopy in Figure 4-3 (a). The Raman spectrum of a triangle WS_2 flake located in the triangles WS_2 in Figure 4-3 (a). It shows that frequency range over 300 cm^{-1} to 600 cm^{-1} with laser excitation at 488 nm was measured at room temperature. The frequency difference between Raman active modes E_{2g}^1 and A_{1g} (Γ) is 63.4 cm^{-1} , indicating that is a bilayer WS_2 [32]. In



addition, the corresponding AFM image of WS₂ was captured with the height profile at 1.8 nm in Figure 4-3 (b). The HR-TEM image in Figure 4-3 (c) confirms the AuNPs with interspacing of 0.23 nm and the HR-TEM image in Figure 4-3 (d) reveals the spatial distribution of AuNPs on the WS₂ crystal. From the HR-TEM image, it is noted that the majority of the AuNPs exist along the edge of the single triangular WS₂.

Measurements of PL spectra and mapping were carried out in a micro-Raman system (Horiba Jobin Yvon HR800) with PL mode. A 100x objective lens with numerical aperture NA of 0.9 was used for the measurement at room temperature. The spot size of laser is about 1 μm. The laser power needs to be set at below ~50 μW to avoid the possible localized heating effect and oxidation from the solid-state laser [51].

It is interesting to investigate how the PL is varied when adding the defective sites on the WS₂ before decoration of AuNPs. In order to study the effect of defective sites on Au nucleation, the laser with power of 0.5 mW was irradiated on the designated bilayer WS₂ flake in 10 min. And then some defect sites may possibly be induced on the bilayer WS₂ when optical activation of the laser on or above 5 μW [126, 127]. Subsequently, it would be started to decorate the AuNPs on that WS₂ sample via the immersion of HAuCl₄⁻ solution process described in section 3.3.1. Accordingly, the Au nucleation on the 2D WS₂ flake should be in favor of those sulfur vacancies. In comparison to the Au/WS₂ nanostructure before laser irradiation, AuNPs arrangement on the irradiated sample is obviously denser in Figure 4-4 (a). The occupations of deposited AuNPs are not only on the edge sites but also in the central part of the WS₂ triangle flake after the laser treatment.



Therefore, AuNPs would be anchored mainly on the surface of WS₂ via the trace of laser irradiation, which is not limited to the edges sites. By counting the numbers of AuNPs in Figure 4-4 (a), there are about 18 to 22 granules of AuNPs within each region. The pairs of AuNPs were labelled with orange circles in Figure 4-4(a). However, due to the resolution limitation of SEM, it is difficult to describe the exact interspacing between AuNPs. It only observes that the separation between AuNPs (d) is smaller than the radius of AuNPs (a). The light emission intensities of PL spectra from position 1 to 5 before and after AuNPs decoration are shown in Figure 4-4 (b). It is apparent that PL enhancement factor varies in different positions and the maximum 8 folded intensity can be achieved in the position 5 in Figure 4-4 (b). In the position 1 and 2, both of them have ~6 folded of PL enhancement. It has a weak relationship between the PL enhancement factor and density of AuNPs over the WS₂ sample as previous reports [99,128]. Nevertheless, there are formations of Au pairs in position 1, 2 and 5. From the literatures reviews [129, 130], while the Au dimers approaching each other, small absorption of Au at the longer wavelength is due to the dipolar feature. It implies that the overall light scattering intensity will be partially compensated by high frequency mode as the result of the satisfaction of frequency sum rule. Therefore, the small interspacing of AuNPs will lead to a shift of spectral features towards longer wavelength because of the strong interaction between single-particle multipoles. This mode is triggered by the separation of AuNPs (d) equal to or less than the radius of AuNPs (a). However, it has been demonstrated that the dipole mode would abruptly disappear for an extreme small value of d due to the extreme charge coupling, so as to suspend the response across

AuNP pair [67]. As the result of a pair of AuNPs matching the condition of d smaller than a , the simulated light absorption spectrum in Figure 4-6 emerges a second resonance peak at ~ 630 nm discussed later. The resonant wavelength shifts to the longer wavelength approaching to the band-gap of semiconducting WS_2 in ~ 2.1 eV. The reason responsible for the observed PL enhancement is shown in Figure 4-4 (b). In addition to the enhancement in PL intensity, a blue shift in PL spectra can be observed when AuNPs decorated on 2D WS_2 . From the experimental discovery in Figure 4-2 (e), it is impossible to induce the H_2O adsorption on bilayer WS_2 . However, the previous simulated results implied that the pair of Au NPs configuration could give rise to a slight spectral blue shift due to plasmonic resonance [54, 129]. Hence, it reveals that a blue shift in the PL emission wavelength in Figure 4-4 (b) may correlate with the AuNPs arrangement.

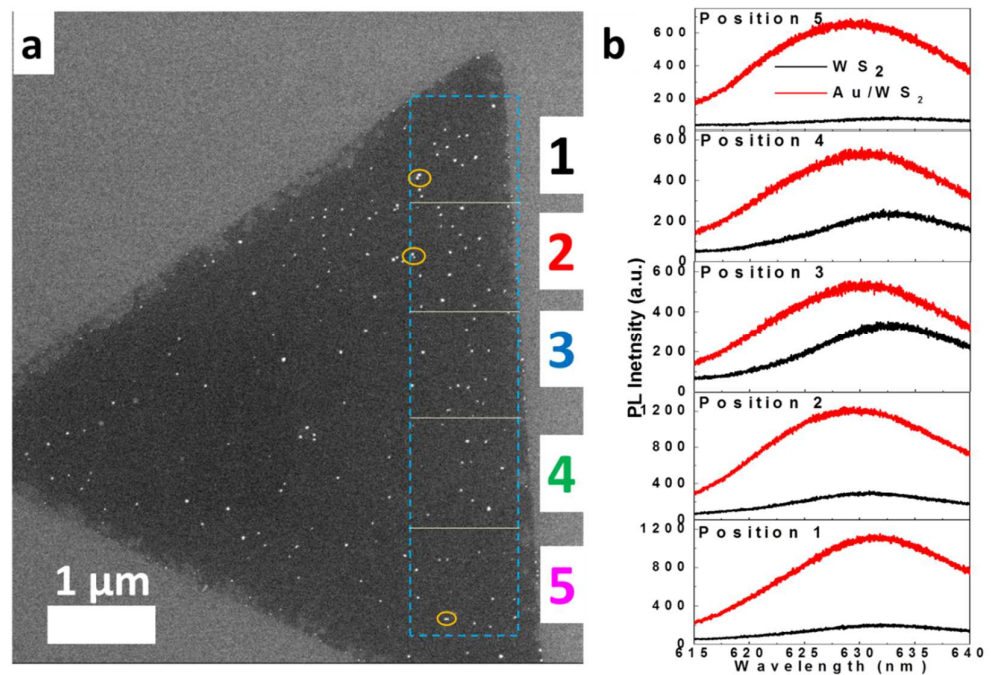


Figure 4-4. (a) The SEM image with labelled position 1-5 corresponding to the PL



THE HONG KONG POLYTECHNIC UNIVERSITY

spectra obtained. (b) PL spectra of position 1-5 before and after the decoration of AuNPs. The pair of AuNPs labelled by the orange circles.

FDTD Solutions 8.9 from Lumerical Solutions was adapted to perform the simulated calculation. In the calculations, total-field scattered-field source (TFSF) was used to launch the electromagnetic pulse in the range of 400-1000 nm into a box containing Au/WS₂ nanostructure. A box of power monitors including total field region was used to calculate the absorption cross section. Also, frequency profile monitors were added in the total field region to calculate the electric field enhancement. Au/WS₂ nanostructure was modeled as an Au sphere/pair of Au sphere with 30 nm in diameter obtained in Figure 4-5 on few layers of WS₂ was taken in the calculation. Referring to the FDTD calculation results, the field profiles with a single Au NP with an averaged diameter of 30 nm and a pair of AuNPs with the same diameter equal to 30 nm separated in a distance of 8 nm and 4 nm are summarized in Figure 4-6. This kind of AuNPs structural configuration can be referred to the TEM image shown in Figure 4-3 (c). The AuNPs with the diameter smaller than 30 nm comparing to the larger excitation wavelength, the contribution of extinction cross section is fully from the dipole absorption of Mie theory. However, when the NPs with the diameter larger than 25 nm, the extinction cross section mainly depends on the higher-order multipole absorption modes in the Mie theory including quadrupole, octopole modes and the scattering. Those high oscillation modes are definitely related to the particles sizes and cause a red-shifted absorption bands because of the increasing NPs sizes. The absorption of total plasmon bands are from superimposing all higher oscillation modes with different energies. However, in this case we only concerns about the separation

between the AuNPs rather than the sizes. Comparing the closely spaced AuNPs both in proximity near 8 nm and 4 nm to a single Au NP, absorbance calculation along the longitudinal excitation (interspacing axis) of pairs of AuNPs reveals two frequencies modes. Furthermore, the enhancement of field is related to the amounts of AuNPs pairs and separations between AuNPs. When shortening the separation between Au NPs, the corresponding absorbance would enhance. There is a tunable resonant frequency at around 630 nm in a pair of AuNPs.

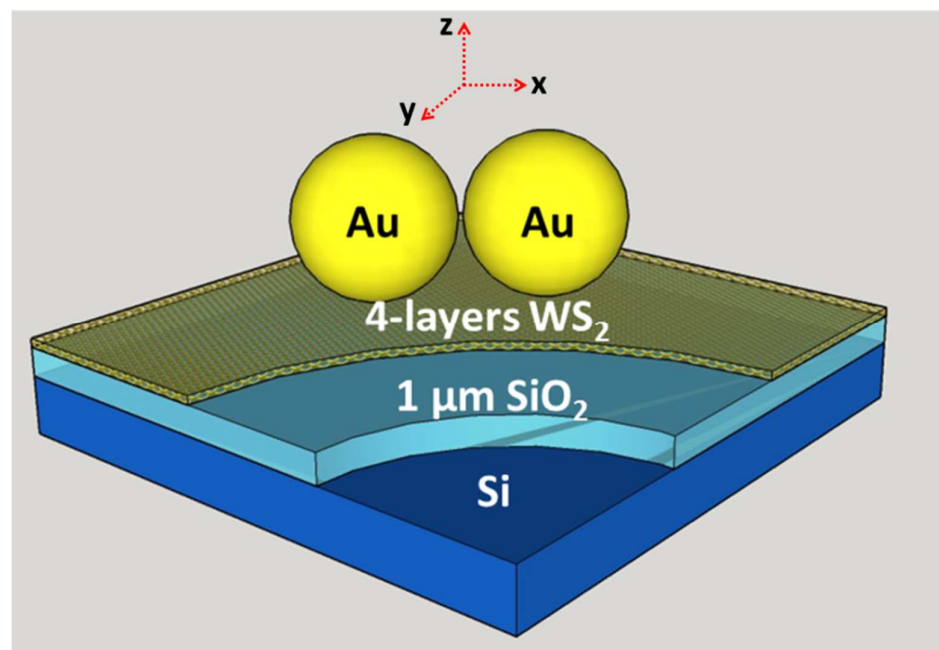


Figure 4-5. The model of AuNP/WS₂ heterostructure modeled by FDTD calculation.

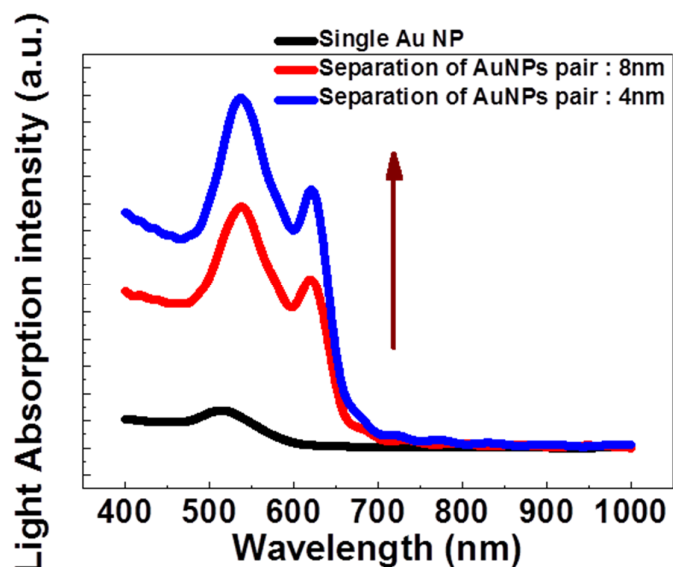


Figure 4-6. Simulated light scattering spectra including a single Au sphere with diameter of 30 nm and a pair of Au-Au sphere both with diameter of 30 nm in the spectral regions of symmetrical surface plasmon mode.

Figure 4-7 shows the theoretical relationship between the intensity enhancements of a single AuNP versus the distance apart from the AuNP on few layers of WS₂. It shows the details in how the AuNP affects the electromagnetic field surrounding WS₂ in dielectric environment. The region shows the maximum enhancement is at ~2 nm separated from single Au NP whereas the intensity enhancement will gradually reduce as far as possible. Within 2 nm spherical region from the AuNP, the effective quenching was induced. It reveals different optical properties of decorating a single AuNP and the pair of AuNPs on bilayer WS₂ hybrid materials.

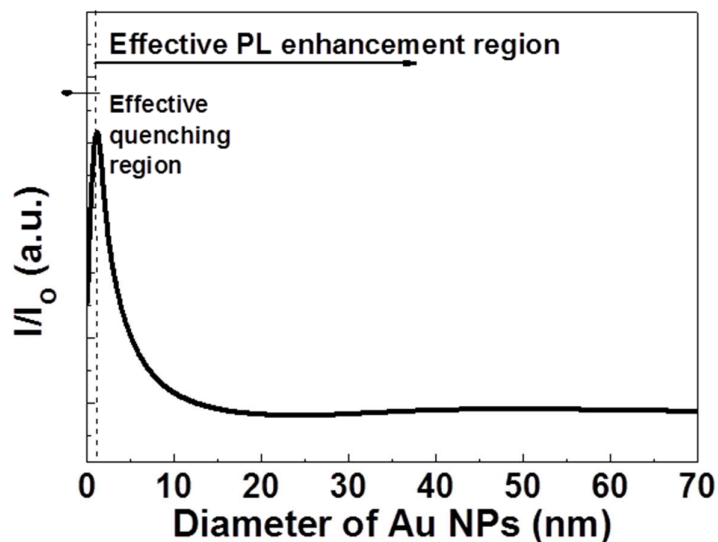


Figure 4-7. The relationship of the intensity enhancement versus interspacing between the AuNPs onto WS₂ calculated theoretically with excitation wavelength at 488 nm.

When AuNPs are in contact with WS₂, metal-semiconducting characteristic typically occurs. Different work functions in AuNPs ($\phi = 3-4$ eV) [131] and bilayer WS₂ ($\phi = 4.2$ in bulk and $\phi = 4.6$ in monolayer) [124] induces an Fermi energy band bending so that n-type doping is suggested. However, Au/WS₂ nanostructure reveals the p-type doping effect from the Raman spectra due to the Raman modes upshifted in Figure 4-8 (a) and (b). The reason is that Au atoms tend to nucleate for the sulfur vacancies sites during Au decoration. After Au atoms nucleated at the sites, it would keep undergoing the aggregation to form of AuNPs. From the previous reports [132], p-type doping of single layer MoS₂ can be established by softening the two Raman active modes especially A_{1g} with a higher sensitivity but not E_{2g}¹. However, due to structural distortion of Raman vibrational A_{1g} and E_{2g}¹ modes causing no effect on symmetrical breakage of

bilayer WS_2 , electrons transferred from semiconducting WS_2 in those electronic states will be placed on bottom conduction band at \mathbf{K} point states which would induce a large degree of electron-phonon coupling. It shows a good agreement with the literature [47].

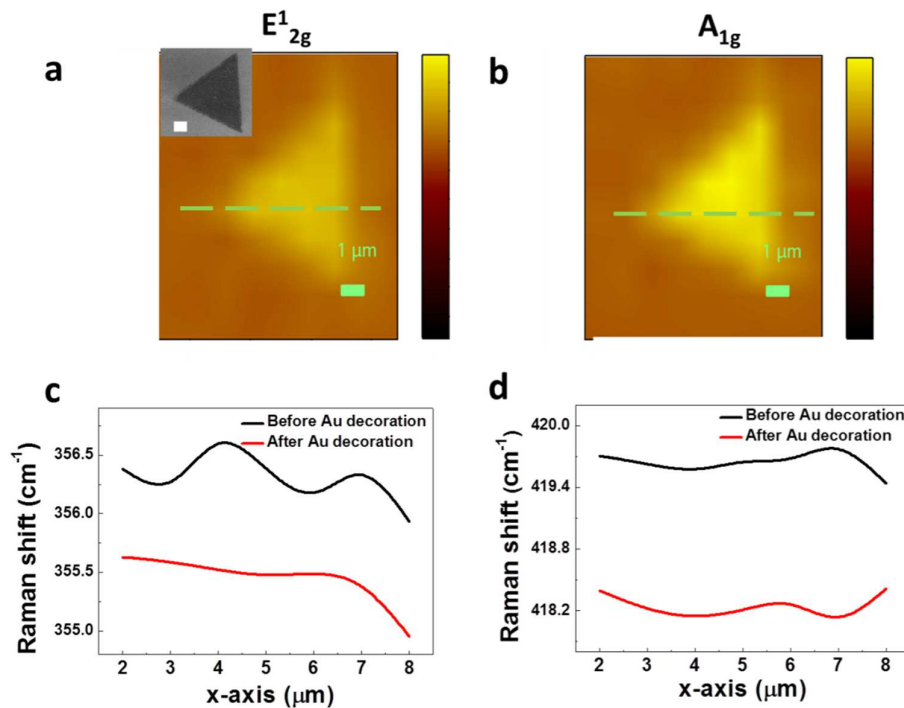


Figure 4-8. (a) Raman mapping of the intensity of the in-plane phonon mode E_{2g}^1 (Γ) before doping AuNPs on the triangular WS_2 flake. (c) The upshift of peak frequency E_{2g}^1 mode under the Lorentzian-fit treatment when doping AuNPs onto bilayer WS_2 crystal. (b) Raman mapping of the intensity of the out-of-plane phonon mode A_{1g} (Γ) before doping AuNPs on the triangular bilayer WS_2 crystal. (d) The upshift of peak frequency A_{1g} modes under the Lorentzian-fit treatment after AuNPs doping. The green dots straight line in (a) and (b) meaning the scanning locus across WS_2 crystal.

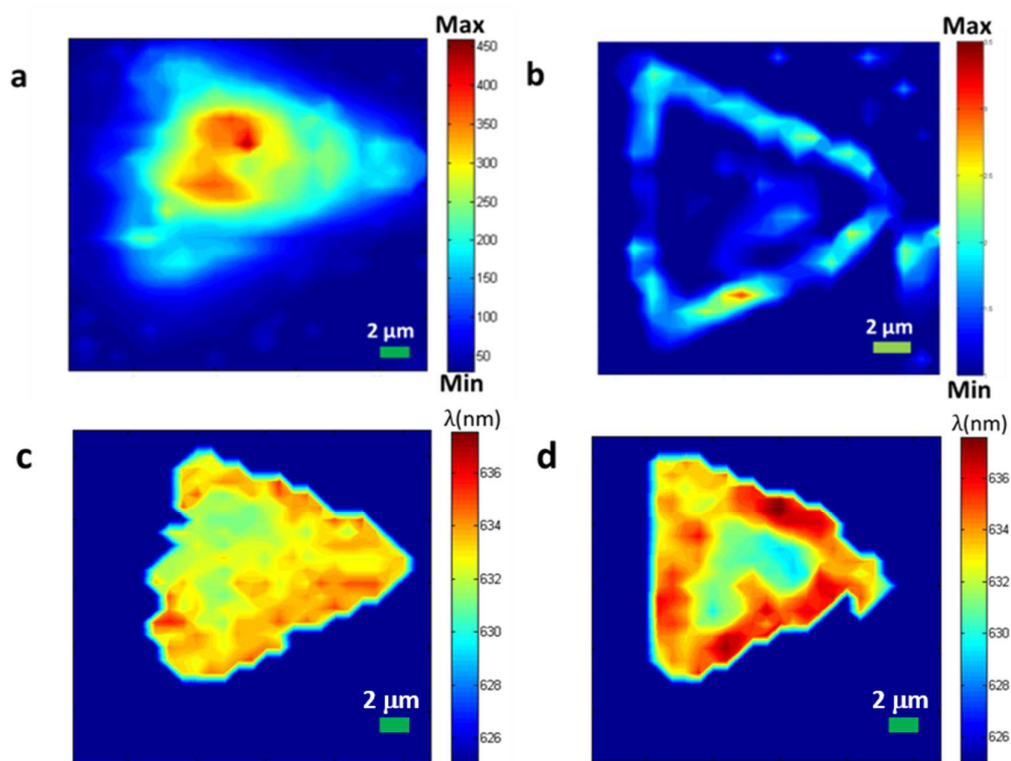
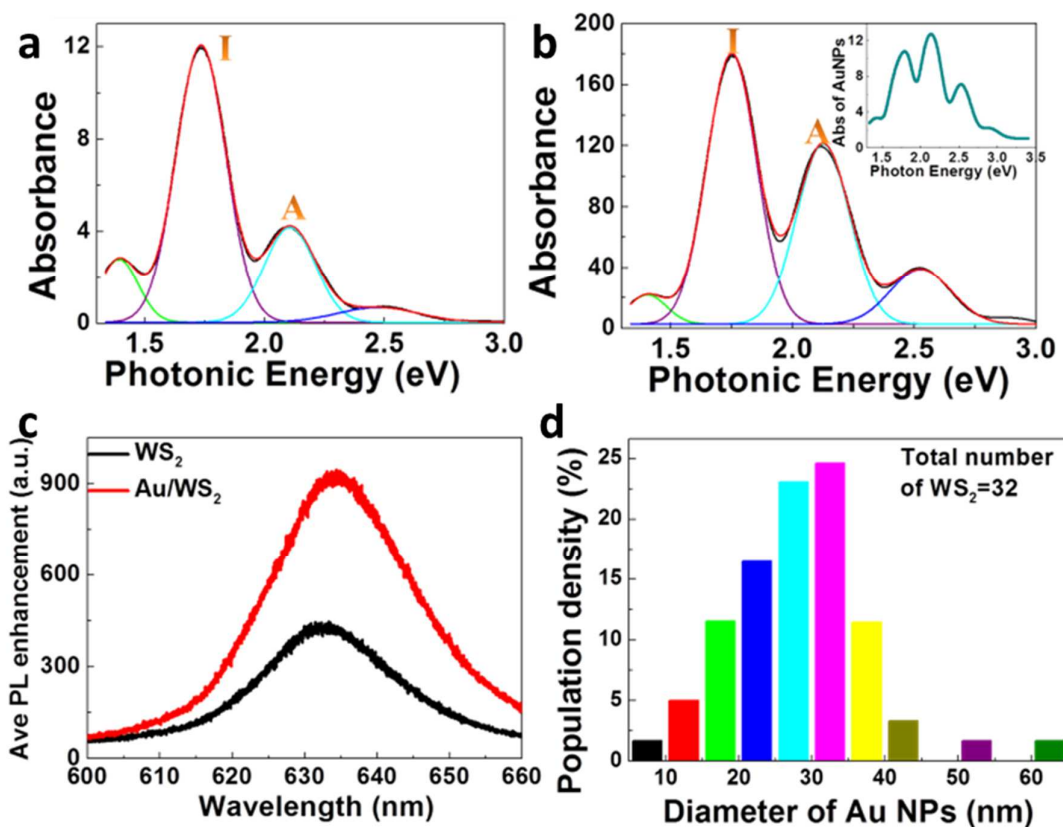


Figure 4-9. Spatial distribution of the PL mapping of a bilayer WS_2 (a) without Au NPs decoration and (b) the overall intensity enhancement I/I_0 comparing with and without AuNPs in the same triangle WS_2 flake. (c) and (d) are the spatial distribution of the peak position mapping of a bilayer WS_2 from (a) and (b).

Figure 4-9 (a) shows the spatial mapping of PL intensity distribution on the surface of a bilayer WS_2 . Figure 4-9 (b) shows the spatial distribution of PL enhancement (I/I_0) of the WS_2 by comparison between with and without AuNPs coating. It can be observed in a range of 1-3 folded enhancement concentrated on the edge sites of WS_2 naturally. It is mainly due to the nucleation of AuNPs over there corresponding to the spatial distribution of AuNPs on triangle WS_2 in Figure 4-9 (b). The average 2-folded PL enhancement of Au/ WS_2 is counted in Figure 4-10 (c). Such a phenomenon can be explained as follows. When WS_2 crystal was

immersed into the aqueous HAuCl_4 solution, the precursor AuCl_4^- ions have more chances to reduce the AuNPs at the edge sites of WS_2 due to the unsaturated sulfur atoms which makes AuNPs easy to anchor on WS_2 as the heterogeneous structure [86, 88, 102]. The AuNPs and WS_2 crystal are in close vicinity which has 2 nm interspacing between Au dimers shown in Figure 4-3 (f). The Au dimers are observed in the whole WS_2 with a less possibility than those AuNPs exists alone. These metal-semiconductor hybrid nanostructures might conduct the exciton-plasmon interaction [106]. According to the spatial mapping of the peak position in Figure 4-9, it reveals the strong red-shift on PL wavelength light emission in AuNPs/bilayer WS_2 nanostructure. However, the explanation on the cause of red-shift light emission is still an open issue.



THE HONG KONG POLYTECHNIC UNIVERSITY

Figure 4-10. (a) and (b) showing the absolute optical absorption spectra of the same bilayer WS₂ flake with labelled excitons I and A representing indirect and direct emission energies from WS₂ crystal with and without AuNPs coating measured at room temperature. The inset of (b) showing the absorbance enhancement in existence of AuNPs. (c) The average PL intensity enhancement extracted from Figure 4-9 (a) and (b). (d) The diameter of Au NPs size distribution estimated by TEM image.

In order to gain an in-depth understanding of the PL enhancement, we have performed the optical absorption measurement on the obtained samples. Figure 4-10 (a) and (b) show the absolute absorption spectra from the WS₂ sample without and with AuNPs decoration. Accordingly, the inset of Figure 4-10 (b) shows the absorbance enhancement in existence of AuNPs. When AuNPs become an amplifier, the light field is enhanced due to the metal nanostructure in the proximity of the 2D semiconducting crystal. A majority of incident photons are absorbed by the Au-WS₂ nano-composites such that the interaction between excitons and plasmons gives rise to a large optical absorption enhancement of the semiconductor WS₂ as shown in Figure 4-10 (b). Enhanced localized electromagnetic field by the MNP from the certain configuration of AuNPs induces the effective optical transition of WS₂ by probably reducing the distance between AuNPs and WS₂.

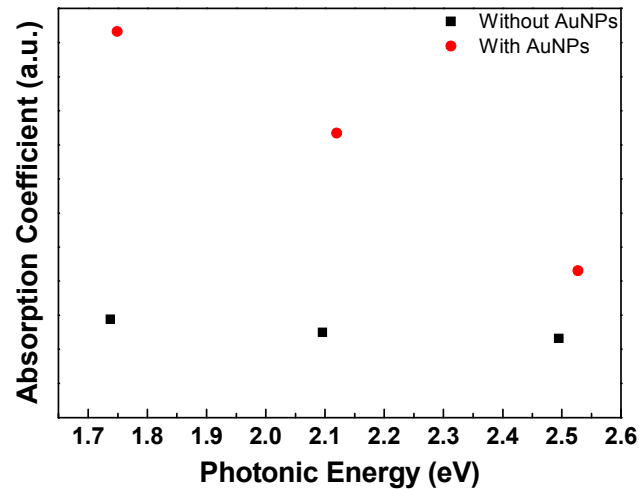


Figure 4-11. The variation of absorption intensity and energies before and after AuNPs decoration.

From Figure 4-10 (a) and (b), it shows a manifest enhancement on light absorption in contrast to the previous absorption spectrum featured a slightly blue shift in the absorption wavelength from 1.73 eV to 1.75 eV and 2.09 eV to 2.12 eV, respectively. It accompanies by the high energy emission and narrower line-width as well shown in Figure 4-11. The narrow line-width in the Au-decorating absorption spectrum also greatly improves the efficiency of light emission of WS₂ due to the arisen LSPR [133]. It can be clearly seen that three prominent resonant frequency peaks arisen by AuNPs are occurred at 490 nm, 580 nm and 690 nm as shown in the inset of Figure 4-10 (b) which can be referred to the size distribution of AuNPs obtained from the TEM images shown in Figure 4-10 (d). According to the previous study [134], the resonant frequency of AuNPs arrangement responding in the visible light region fully matches the light emission of semiconducting bilayer WS₂ crystal. While comparing the spectral peak

wavelength of bare WS₂ and Au/WS₂ nanostructure in Figure 4-10 (a) and (b), there is no any spectral blue shift being able to observe. The previous report has explored that how H₂O makes an large influence on monolayer WS₂ [105]. By the coupled H₂O molecules adsorbed to WS₂ unit cell, it would cause the PL changes due to electron transfer from the coupled molecules so as to enhance the intensity of X but not X⁻. Although the DI water as the solvent of aqueous solution HAuCl₄⁻, it doesn't appear the spectral variation on the proportion in X and X⁻ in the AuNPs decoration onto bilayer WS₂.

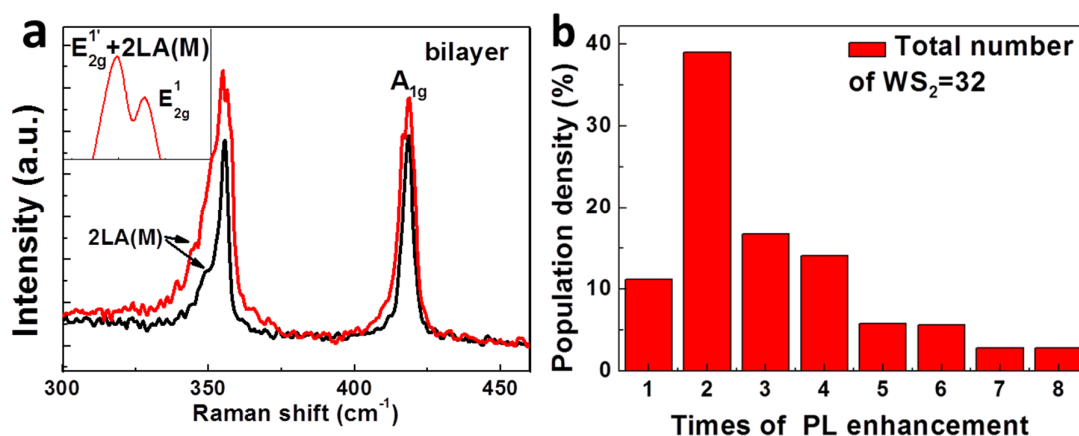


Figure 4-12. (a) Raman spectrum of the same bilayer WS₂ from the Figure 4-3 before (black line) and after (red line) decoration of AuNPs. This spectrum collected by 488 nm excitation wavelength. The inset showing the enlarged graph of the splitting Raman mode E_{2g}¹ with Lorentzian fit. (b) The statistical distribution of average PL enhancement from total 32 Au-WS₂ flakes.

Apart from the study of PL enhancement from the above described in the same single triangle flake, the corresponding Raman spectrum of the same bilayer Au/WS₂ nanostructure was collected in Figure 4-12(a). It gives a weak strain-



induced feature indicated by the Raman mode splitting originated from the mechanical strain in the AuNPs decorated bilayer WS₂ as the literature [100]. It rises redshift of the Raman mode in E¹_{2g} labelled as E^{1'}_{2g} comparing with the originated E¹_{2g}. The redshift between E^{1'}_{2g} and E¹_{2g} is about 1.6 cm⁻¹ in AuNPs/bilayer WS₂. Now PL variations from more triangle bilayer flakes were measured to get the average PL enhancement on experiencing the laser irradiation. Figure 4-12 (b) shows the average PL enhancement by decorating AuNPs on total 32 pieces of bilayer triangle WS₂ in the same sample in Figure 4-3 (a). By examining the bilayer WS₂ with Raman spectroscopy, those bilayer triangles WS₂ flake were needed to be chosen to facilitate the LSPR effect on the PL enhancement by decorating AuNPs on a large amount of WS₂. Also the PL spectrum measurements were undergone by locating laser excitation on the center of triangle WS₂ flakes. From the statistical analysis shown in Figure 4-12 (b), we found that over 80% of AuNPs/WS₂ nanostructure induced PL enhancement on or over two-folded on the whole, further supporting the feasibility of enhancing PL via the simple method of decorating Au NPs on bilayer WS₂.

In a brief summary, we have performed the synthesis, structural and PL characterization of Au-WS₂ nanostructure. AuNPs can be selectively anchored on the surface of edge and defective sites of triangle atomic layered WS₂. The conjugate provides an opportunity to modify PL features of 2D material due to increased optical absorption by plasmonic effect. We have demonstrated an enhancement and spatial distribution of PL in the Au/bilayer WS₂ nanostructure which is closely related to the separation between AuNPs to arise by the strength of dipolar feature triggered by d equal to or smaller than a . The simple method of

Au NPs decoration may be generally expanded to the PL enhancement in a variety of 2D materials, which may provide a material platform to improve and exploit nanoscale photonic devices.

4.1.2. Au/WS₂ nanostructure from AuNRs coating

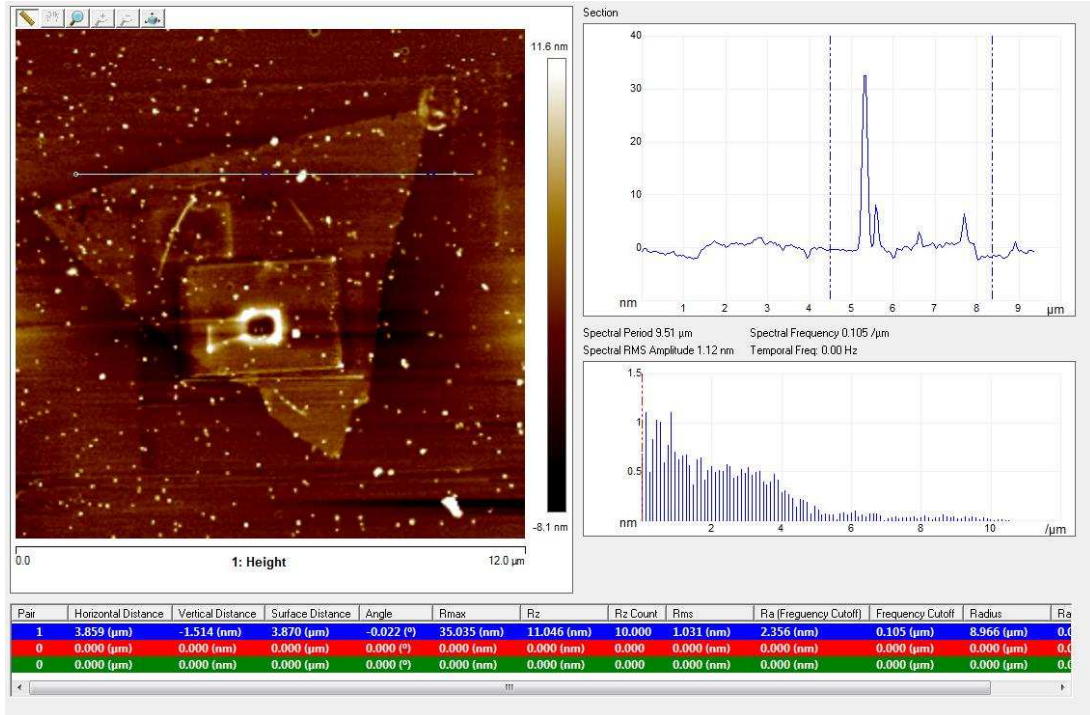


Figure 4-13. AFM image of AuNR/bilayer WS₂ with height profile along with the labelled scanning axis.

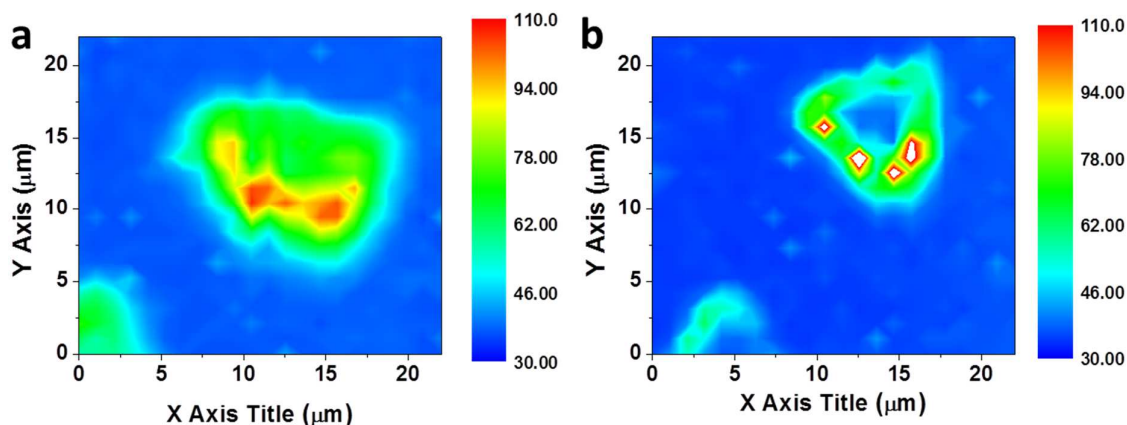


Figure 4-14. Spatial distribution of the PL mapping of a bilayer WS_2 (a) before and (b) after Au NPs decoration.

The synthesized AuNRs were characterized first (described in section 3.2.2) and then coated on the bilayer WS_2 demonstrated in height profile of Figure 4-12 at 1.514 nm. The as-prepared sample was used to compare whether the different AuNPs morphology deposited on the 2D materials will vary the optical property or not. From the spatial distribution of PL intensity mapping in Figure 4-13, it shows that the light emission from central body in bilayer WS_2 quenches greatest compared to that at the edges. However, it is clear that the observation of rectangle prominence at the center of triangle WS_2 in Figure 4-12. It is due to the residue surfactant on the sample undergoing SEM characterization in which the high energetic electron beam hitting on the WS_2 charges up the sample so as to leave a large thrust area. Although the PL mapping shows a slightly enhancement, residual inorganic materials cause inaccurate optical efficiency.

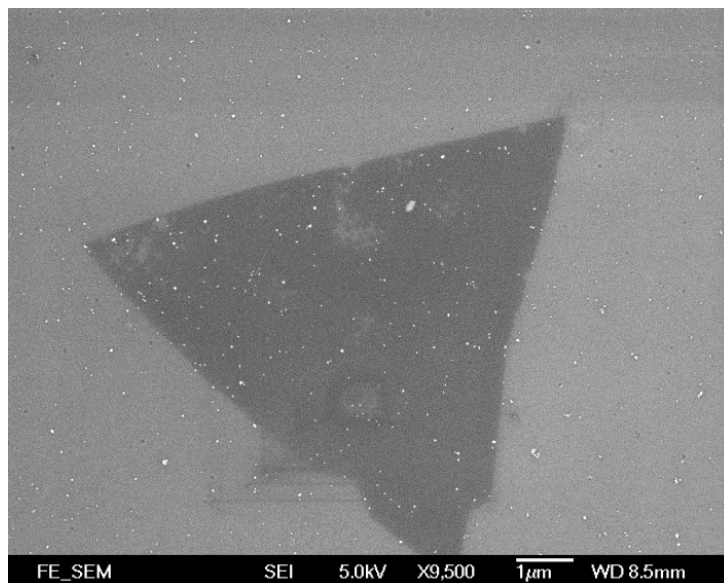


Figure 4-15. SEM characterization.

In summary, using the synthesized AuNRs decorated onto WS₂ would cause some residues arisen from surfactants which is the ingredient used in the AuNRs synthesis process. It would lead to the unknown effect on the measurement of PL emission. Also, the decorated sample had been immersed into water to allow the surfactant resolvable in DI water. However, little amount of surfactant would still adsorb on the surface of WS₂. The surfactant may cause deterioration on the PL spectrum. It has been difficult to get rid of the remaining surfactant completely.

4.1.3. Au/WS₂ nanostructure from AuNPs annealing

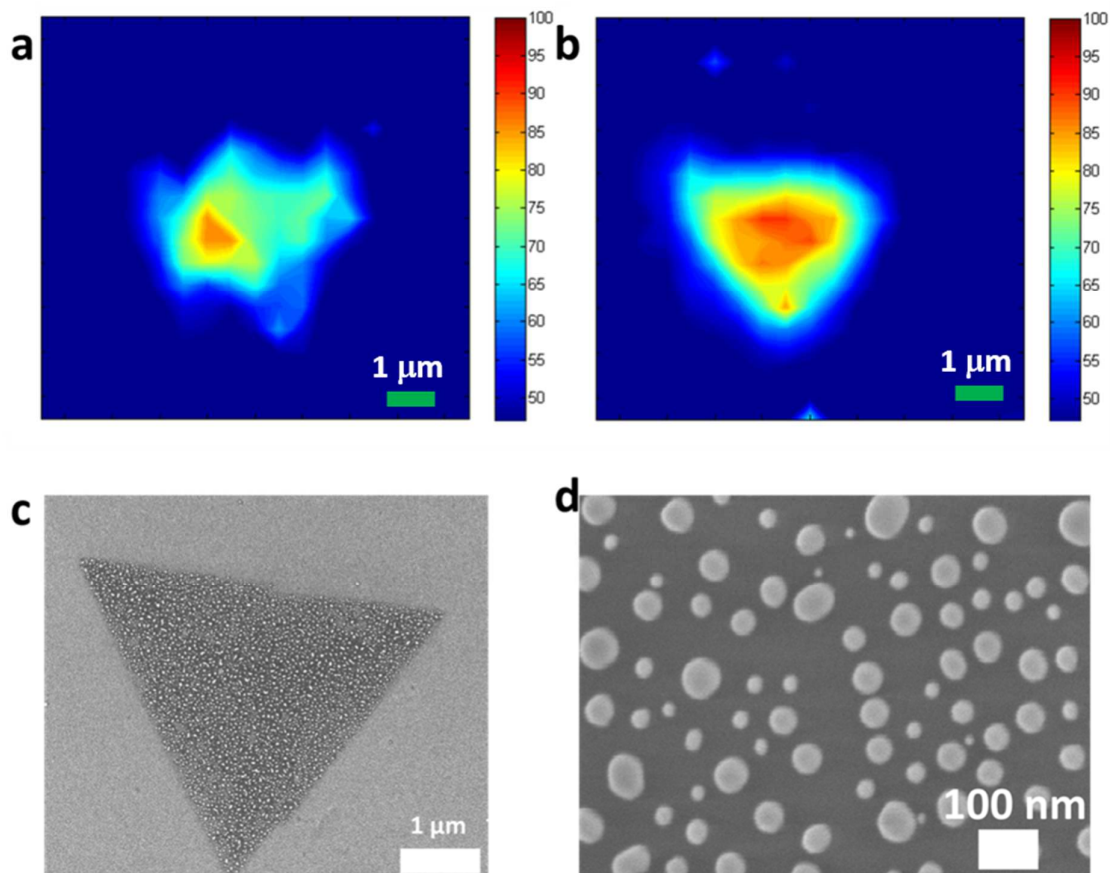


Figure 4-16. (a) Spatial distribution of the PL mapping of a bilayer WS₂ (a) before and (b) after Au NPs annealing. (c) SEM images characterization. (d) The enlarged image captured by SEM.

The fabrication of AuNPs by thermal evaporating Au film and then annealing can control the density of AuNPs deposited on the surface of WS₂. The advantage of Au film evaporated on WS₂ by thermal evaporation is due to the non-defective deposition on 2D materials. By controlling the thickness of the film deposited and the annealing temperature, the sizes distribution of the AuNPs can be precisely adjusted. However, it is only able to vary the size but not the separation between the AuNPs. In Figure 4-15(a), the PL mapping cannot reflect

the shape of triangle WS_2 flake. However, after AuNPs deposited onto WS_2 , the localized field enhancement helps concentrate the light emission from the sample so that it reveals the coincided PL intensity with the bilayer triangle WS_2 flake. On the other hand, it is easy for quenching due to configuration of denser and closely spaced AuNPs. There are much non-coincident AuNPs sizes with a wide-range distribution adhered on the surface of WS_2 . It is found that the smooth WS_2 surface has narrower sizes distribution of AuNPs than that for rough surface. It indicates that not only annealing temperature/metal thickness but also the smoothing of WS_2 surface can control the sizes/shape distribution of AuNPs.

To summarize, the hybrid Au/ WS_2 crystal through film annealing method cannot be well controlled the average morphologies and sizes of the AuNPs. The sizes of AuNPs are highly related to those parameters, such as annealing temperatures, thickness of evaporated film and smoothing of WS_2 surface.

4.2. PL quenching from Au film/ WS_2 nanostructure

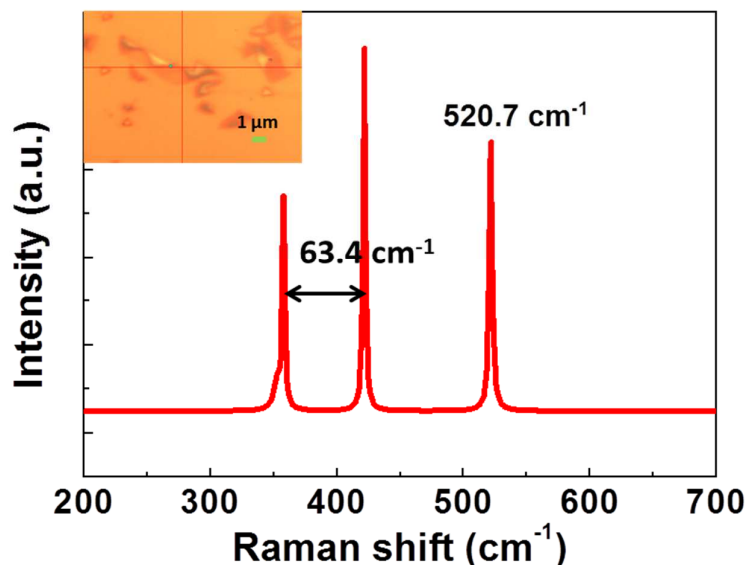


Figure 4-17. Raman spectrum of Au/ WS_2 hybrid system with a labelled Si peak as

a reference. The inset showing the OM image of the as-prepared Au/WS₂ system.

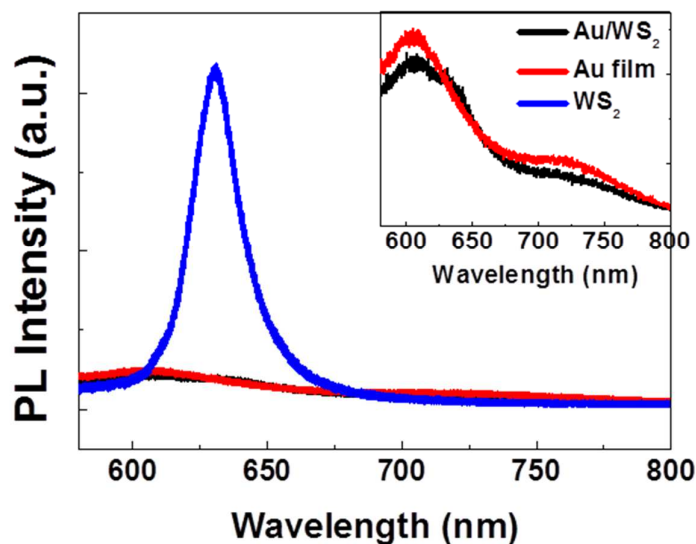


Figure 4-18. The PL spectra corresponding to WS₂, Au/WS₂ and Au film. The inset showing the enlarged PL spectra of Au film and Au/WS₂ heterostructure ranging from 580 nm to 800 nm, respectively.

First, the prepared WS₂ was transferred using PMMP with molecular weight of 950 K brought from MicroChem. PMMA was spin-coated with first at 500 rpm for 10 s and second at 300 rpm for 30 s. After that, the sample was baked at 100 °C for 10 min and then put into 1M NaOH for 15 min. Finally, the PMMA-capped WS₂ washed by DI water to remove all chemicals residues [135]. The PMMA-capped WS₂ was put onto the Si substrate with sputtered Au film and heating at around 80 °C to drive out the water moisture. The adhesion between WS₂ and Au surface is enhanced. Figure 4-16 reveals the OM image after transferred sample onto Au film and the Raman spectrum was obtained from laser focusing on the central area of the OM image. The Raman spectrum of bilayer WS₂ with active E_{2g} and A_{1g} modes at 357.56 cm⁻¹ and 420.96 cm⁻¹. It shows a little bit shifting towards longer wavelength after transferring. This variation is

due to the change of interface between WS_2 and SiO_2/Au . The doping mechanism due to charge transfers from WS_2 to Au will be directly related to the electron density and the stiffening of the Raman A_{1g} mode [136]. The corresponding surface details of sputtered Au film have been shown in Figure 4-17.

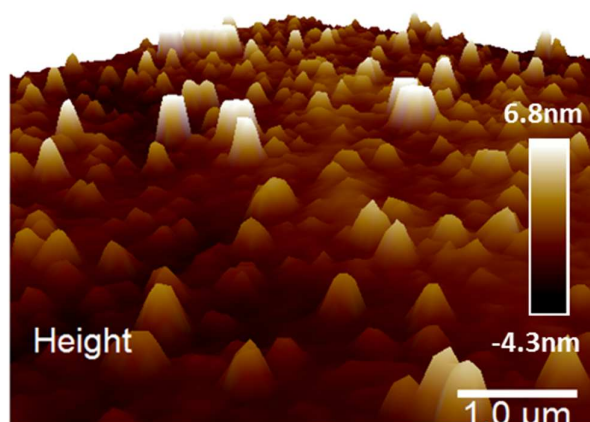


Figure 4-19. High resolution AFM image of Au film on Si substrate.

The mean value of Au film roughness deposited by sputtering system was characterized in 1.4 nm. Figure 4-18 shows the PL spectra correlated to bare sputtered Au film, Au/bilayer WS_2 and bare WS_2 flake.

The PL measurements were performed among the nanostructures of Au film, bilayer WS_2 and Au/bilayer WS_2 . In contrast to the structures between bilayer WS_2 and Au/ WS_2 hybrid materials, the PL intensities are highly quenched after formation of Au/ WS_2 . It is obvious that the similar PL intensities occur with and without WS_2 on the deposited Au film on the inset of Figure 4-17. It is due to the interaction of the charge transfers between the Au film and WS_2 flake. It can

be deduced that the PL quenching due to the Au nanostructure relevant to the variation of electronic band structure in Figure 4-18. The Fermi levels of monolayer WS_2 and Au film were reported in ~ 4.6 eV and 5.1 eV [137] respectively. There is an offset Fermi level at ~ 0.5 eV and bands bending when the contact established between Au and WS_2 . When the valence band electrons excited to the conduction band energy levels in WS_2 under illumination, the holes remain in the valence bands and excited electrons transfer towards the Au layers. P-type doping effect appears in WS_2 by reducing amount of electrons in valence bands such that PL quenching occurs in the Au/ WS_2 nanostructure.

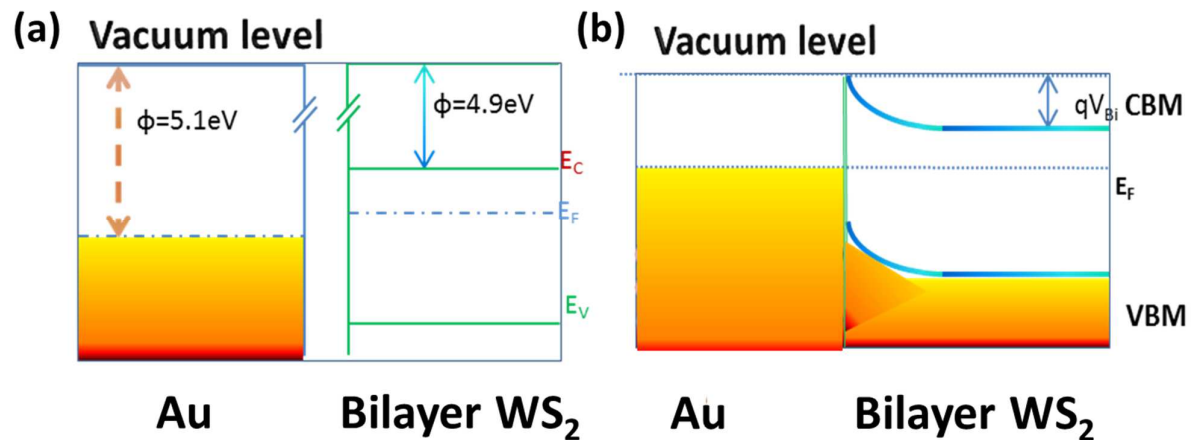


Figure 4-20. Energy band diagrams of Au/ WS_2 (a) and (b) showing the electron transfer mechanism in hybrid Au/ WS_2 system before and after contact establishments respectively.

4.3. Summary

The hybrid Au/ WS_2 materials have been formed by three different AuNPs synthesized methods to produce the desirable 2D nanostructures including



immersion of WS₂ sample into aqueous HAuCl₄⁻ solution, annealing gold film by thermal evaporation and seed-method synthesis of NRs. Those gold nanostructures were synthesized with different emissions of resonant frequencies attributed to morphologies so that it causes influence on the corresponding PL emission. The reason why bilayer WS₂ was adopted instead of monolayer is due to the highly influencing effect by H₂O molecules adsorbed to monolayer WS₂ causing electron transfers. According to the synthesized method with HAuCl₄⁻, the AuNPs nucleated on the intrinsic defective sites of WS₂ which have uncontrollable distribution during different experimental conditions such as the evaporation temperature of sulphur powders as well as the furnace temperature during the reaction, etc. However, many techniques such as laser irradiation have been adopted to process some extrinsic defects after fabrication of 2D materials. After laser irradiation, the sample was dipped into HAuCl₄⁻ solution. It is found that the existences of a pair of AuNPs are in a small friction. And the pair structure of AuNPs causes a highly enhanced PL producing the LSPR effect. The existences of AuNP were demonstrated according to the absorption spectrum and HRTEM characterization.

Also, the AuNPs fabrication by annealing the Au evaporated film has been adsorbed onto the WS₂. This experiment has been initially used to observe the effect due to the average size distribution of AuNPs but uncontrollable in random separations. However, it has shown that the parameters influenced the formation of morphologies/sizes of AuNPs are dependent on the roughness of the surface of WS₂ crystals. The uneven WS₂ surface induces different sizes distribution of annealed AuNPs to measure the effect on PL measurement only arisen from the



change between AuNPs separations.

The third method is mainly due to the as-synthesized AuNRs coating onto WS₂ samples. The change of morphological observation through SEM and AFM images can be revealed that the residues of surfactant are hard to remove only by DI water completely. Those remaining residues are the uncertainty responsible for the effect of PL emission.

In this part, the studies on both the changes in morphologies of AuNPs and verifies the Au film affecting the PL emission via the Au film/WS₂ hybrid materials are carried out. In contrast to the previous reports from other scientists, it had been proven that the Au film quenching could result in the PL emission from WS₂.





Chapter 5. Conclusions and Suggestions for Future Work

5.1. Conclusions

Atomically thin layers of WS₂ were prepared by the sulfurization of sputtered tungsten film and AuNPs were used to decorate the surface of such 2D layers. The sputtered tungsten film was prepared at few nanometers thick. The few-layered WS₂ was measured fabricated through various characterization techniques, such as SEM, TEM, Raman and PL spectroscopies. From the SEM and TEM results, it is shown that the fabrication can result in the predominant bilayer WS₂ in the average sizes of 20 μm. The Raman spectrum of bilayer WS₂ was measured and active E²_{1g} and A_{1g} modes at 357.56 cm⁻¹ and 420.96 cm⁻¹ were observed. The experimental conditions for these triangles WS₂ were performed by gradually ramping to 750°C for 10 minutes during the reaction with H₂/Ar gas flowing. By fabricating the hybrid nanostructures of AuNPs/WS₂, optical properties of the as-prepared samples have been investigated in this thesis.

There are three various methods for the synthesis of gold nanostructures with different morphologies. These methods described in the fabrication of AuNPs nanostructures include the preparation of HAuCl₄⁻ aqueous solution, annealing of thin Au film and chemical synthesis of AuNRs. The fabricated hybrid AuNPs/WS₂ nanostructures can generate different optical properties.

Firstly, hybrid structure of AuNPs/WS₂ was fabricated by immersion of HAuCl₄⁻ aqueous solution. The as-prepared sample can induce p-type doping effect in WS₂ layer by analyzing the upshift of softening Raman vibrational modes



of $E_{1'_{2g}}$ and A_{1g} . The redshift between $E_{1'_{2g}}$ and $E_{1_{2g}}$ is about 1.6 cm^{-1} in Au/bilayer WS_2 . This can be attributed to the metallic AuNPs–semiconductor WS_2 contact establishment causing electron transfer from semiconductor to metal by the driving force arisen by different Fermi energy level of WS_2 . Furthermore, in contrast to the absorption spectra before and after Au decorations, the excitons I and A have experienced a slight blue-shift which are from 1.73 eV to 1.75 eV and 2.09 eV to 2.12 eV.

Secondly, the decoration of WS_2 via immersion of HAuCl_4^- solution with higher concentration would raise the possibility of AuNPs nucleation other than affecting the aggregations of AuNPs. Afterwards, the interspacing of AuNPs onto WS_2 crystal can be modified at least a few nanometers to amplify the light emission in 8-folded at maximum. Besides, the sizes of AuNPs can be tuned by altering the thickness of Au evaporated film and annealing temperature. The roughness on the surface of WS_2 will cause a quite wide range for the sizes of AuNPs distribution.

Thirdly, the further investigation on the PL of Au/ WS_2 hybrid materials indicates exciton-plasmon interaction is highly related to spatial distribution of AuNPs. In contrast to the absorption spectra of WS_2 before and after AuNPs decorations, PL enhancement can be revealed by the enhancement of peak intensities and narrowing of the FWHM. The FDTD calculated result shows the second frequencies dipolar enhancement while separation between AuNPs $a < d$ diameter of AuNPs at 630 nm.

In conclusion, the desirable PL with the largest 8-folded enhancement can be achieved via the AuNPs decoration from immersion of aqueous HAuCl_4^-



chemical solution. This finding related to fundamental physics can make investigations on LSPR between 2D WS₂ and configuration with different morphologies of AuNPs. Moreover, the plasmon enhanced optical properties can boost in developing the applications for optoelectronic and optical devices based on light-to-current conversion.

5.2. Suggestions for the future work

In this project, the surface plasmon enhanced optical properties of hybrid Au/WS₂ system have been characterized through the PL and absorption spectroscopy. Some suggestions for the further researches are listed as follow, which can be regarded as the further improvement of present works in the future:

In comparison to WS₂ before Au decorations, WS₂ after decoration clearly shows the enhancement of PL. And then the FDTD calculation modelled by the special arrangements of AuNPs observed from TEM images coincides with the pervious results. Further investigations should provide solid evidences to explain the experimental results in details. For example, the measurement of scanning near-field microscopy (SNOM) can give the information of sample arisen by LSPR. In addition, the adoption of nano-Fourier Transform Infrared (nano-FTIR) spectroscopy for scanning the configurations of AuNPs is suggested to provide the precise changes of absorption spectra between the interspacing of AuNPs down to the nano-scale.



References

- [1] L. D. Landau, E. M. Lifshits and L. P. Pitaevskiĭ, *Statistical Physics*, 3rd ed. (Pergamon Press, New York, 1980).
- [2] N. D. Mermin, *Physical Review* **176** (1), 250-254 (1968).
- [3] K. S. Novoselov, A. K. Geim, S. V. Morozov, D. Jiang, Y. Zhang, S. V. Dubonos, I. V. Grigorieva and A. A. Firsov, *Science* **306** (5696), 666-669 (2004).
- [4] C. N. R. Rao, A. K. Sood, K. S. Subrahmanyam and A. Govindaraj, *Angewandte Chemie International Edition* **48** (42), 7752-7777 (2009).
- [5] R. F. Frindt, *Journal of Applied Physics* **37** (4), 1928-1929 (1966).
- [6] P. Joensen, R. F. Frindt and S. R. Morrison, *Materials Research Bulletin* **21** (4), 457-461 (1986).
- [7] V. Nicolosi, M. Chhowalla, M. G. Kanatzidis, M. S. Strano and J. N. Coleman, *Science* **340** (6139) (2013).
- [8] J. N. Coleman, M. Lotya, A. O'Neill, S. D. Bergin, P. J. King, U. Khan, K. Young, A. Gaucher, S. De, R. J. Smith, I. V. Shvets, S. K. Arora, G. Stanton, H.-Y. Kim, K. Lee, G. T. Kim, G. S. Duesberg, T. Hallam, J. J. Boland, J. J. Wang, J. F. Donegan, J. C. Grunlan, G. Moriarty, A. Shmeliov, R. J. Nicholls, J. M. Perkins, E. M. Grieverson, K. Theuwissen, D. W. McComb, P. D. Nellist and V. Nicolosi, *Science* **331** (6017), 568-571 (2011).
- [9] L. F. Mattheiss, *Physical Review Letters* **30** (17), 784-787 (1973).
- [10] J. Zheng, H. Zhang, S. Dong, Y. Liu, C. Tai Nai, H. Suk Shin, H. Young



THE HONG KONG POLYTECHNIC UNIVERSITY

- Jeong, B. Liu and K. Ping Loh, *Nature Communication* **5** (2995), (2014).
- [11] RadisavljevicB, RadenovicA, BrivioJ, GiacomettiV and KisA, *Nature Nanotechnology* **6** (3), 147-150 (2011).
- [12] D. Jariwala, V. K. Sangwan, L. J. Lauhon, T. J. Marks and M. C. Hersam, *ACS Nano* **8** (2), 1102-1120 (2014).
- [13] S. Z. Butler, S. M. Hollen, L. Cao, Y. Cui, J. A. Gupta, H. R. Gutiérrez, T. F. Heinz, S. S. Hong, J. Huang, A. F. Ismach, E. Johnston-Halperin, M. Kuno, V. V. Plashnitsa, R. D. Robinson, R. S. Ruoff, S. Salahuddin, J. Shan, L. Shi, M. G. Spencer, M. Terrones, W. Windl and J. E. Goldberger, *ACS Nano* **7** (4), 2898-2926 (2013).
- [14] F. Schwierz, *Nature Nanotechnology* **5** (7), 487-496 (2010).
- [15] C. H. Lui, Z. Li, K. F. Mak, E. Cappelluti and T. F. Heinz, *Nature Physics* **7** (12), 944-947 (2011).
- [16] A. K. Geim and K. S. Novoselov, *Nature Materials* **6** (3), 183-191 (2007).
- [17] K. S. Novoselov, A. K. Geim, S. V. Morozov, D. Jiang, M. I. Katsnelson, I. V. Grigorieva, S. V. Dubonos and A. A. Firsov, *Nature* **438** (7065), 197-200 (2005).
- [18] Z. Qiao, W. Ren, H. Chen, L. Bellaiche, Z. Zhang, A. H. MacDonald and Q. Niu, *Physical Review Letters* **112** (11), 116404 (2014).
- [19] A. S. Mayorov, R. V. Gorbachev, S. V. Morozov, L. Britnell, R. Jalil, L. A. Ponomarenko, P. Blake, K. S. Novoselov, K. Watanabe, T. Taniguchi and A. K. Geim, *Nano Letters* **11** (6), 2396-2399 (2011).
- [20] A. A. Balandin, S. Ghosh, W. Bao, I. Calizo, D. Teweldebrhan, F. Miao and C. N. Lau, *Nano Letters* **8** (3), 902-907 (2008).



THE HONG KONG POLYTECHNIC UNIVERSITY

- [21] Y. Zhang, Y.-W. Tan, H. L. Stormer and P. Kim, *Nature* **438** (7065), 201-204 (2005).
- [22] H. R. Gutiérrez, N. Perea-López, A. L. Elías, A. Berkdemir, B. Wang, R. Lv, F. López-Urías, V. H. Crespi, H. Terrones and M. Terrones, *Nano Letters* **13** (8), 3447-3454 (2013).
- [23] A. Molina-Sánchez and L. Wirtz, *Physical Review B* **84** (15), 155413 (2011).
- [24] L. Kulyuk, D. Dumcehniko, E. Bucher, K. Friemelt, O. Schenker, L. Charron, E. Fortin and T. Dumouchel, *Physical Review B* **72** (7), 075336 (2005).
- [25] S. Jo, N. Ubrig, H. Berger, A. B. Kuzmenko and A. F. Morpurgo, *Nano Letters* **14** (4), 2019-2025 (2014).
- [26] E. J. Sie, J. W. McIver, Y.-H. Lee, L. Fu, J. Kong and N. Gedik, *Nature Materials* **14** (3), 290-294 (2015).
- [27] H. Zeng, J. Dai, W. Yao, D. Xiao and X. Cui, *Nat Nano* **7** (8), 490-493 (2012).
- [28] Z. Yang, D. Gao, J. Zhang, Q. Xu, S. Shi, K. Tao and D. Xue, *Nanoscale* **7** (2), 650-658 (2015).
- [29] J. Heising and M. G. Kanatzidis, *Journal of the American Chemical Society* **121** (4), 638-643 (1999).
- [30] S. Jo, D. Costanzo, H. Berger and A. F. Morpurgo, *Nano Letters* **15** (2), 1197-1202 (2015).
- [31] A. Chernikov, T. C. Berkelbach, H. M. Hill, A. Rigosi, Y. Li, O. B. Aslan, D. R. Reichman, M. S. Hybertsen and T. F. Heinz, *Physical Review*



THE HONG KONG POLYTECHNIC UNIVERSITY

- Letters **113** (7), 076802 (2014).
- [32] A. Berkdemir, H. R. Gutierrez, A. R. Botello-Mendez, N. Perea-Lopez, A. L. Elias, C.-I. Chia, B. Wang, V. H. Crespi, F. Lopez-Urias, J.-C. Charlier, H. Terrones and M. Terrones, *Sci. Rep.* **3** (2013).
- [33] A. Ramasubramaniam, *Physical Review B* **86** (11), 115409 (2012).
- [34] P. K. Nayak, C.-H. Yeh, Y.-C. Chen and P.-W. Chiu, *ACS Applied Materials & Interfaces* **6** (18), 16020-16026 (2014).
- [35] K. F. Mak, C. Lee, J. Hone, J. Shan and T. F. Heinz, *Physical Review Letters* **105** (13), 136805 (2010).
- [36] A. Splendiani, L. Sun, Y. Zhang, T. Li, J. Kim, C.-Y. Chim, G. Galli and F. Wang, *Nano Letters* **10** (4), 1271-1275 (2010).
- [37] G. L. Frey, S. Elani, M. Homyonfer, Y. Feldman and R. Tenne, *Physical Review B* **57** (11), 6666-6671 (1998).
- [38] D. Ovchinnikov, A. Allain, Y.-S. Huang, D. Dumcenco and A. Kis, *ACS Nano* **8** (8), 8174-8181 (2014).
- [39] W. Sik Hwang, M. Remskar, R. Yan, V. Protasenko, K. Tahy, S. Doo Chae, P. Zhao, A. Konar, H. Xing, A. Seabaugh and D. Jena, *Applied Physics Letters* **101** (1), 013107 (2012).
- [40] C. Lee, H. Yan, L. E. Brus, T. F. Heinz, J. Hone and S. Ryu, *ACS Nano* **4** (5), 2695-2700 (2010).
- [41] G. Eda, H. Yamaguchi, D. Voiry, T. Fujita, M. Chen and M. Chhowalla, *Nano Letters* **11** (12), 5111-5116 (2011).
- [42] H. S. S. Ramakrishna Matte, A. Gomathi, A. K. Manna, D. J. Late, R. Datta, S. K. Pati and C. N. R. Rao, *Angewandte Chemie International*



THE HONG KONG POLYTECHNIC UNIVERSITY

Edition **49** (24), 4059-4062 (2010).

- [43] J. V. Lauritsen, J. Kibsgaard, S. Helveg, H. Topsoe, B. S. Clausen, E. Laegsgaard and F. Besenbacher, *Nature Nanotechnology* **2** (1), 53-58 (2007).
- [44] Y. Zhan, Z. Liu, S. Najmaei, P. M. Ajayan and J. Lou, *Small* **8** (7), 966-971 (2012).
- [45] Y.-H. Lee, X.-Q. Zhang, W. Zhang, M.-T. Chang, C.-T. Lin, K.-D. Chang, Y.-C. Yu, J. T.-W. Wang, C.-S. Chang, L.-J. Li and T.-W. Lin, *Advanced Materials* **24** (17), 2320-2325 (2012).
- [46] A. D. Brothers and J. B. Brungardt, *physica status solidi (b)* **91** (2), 675-679 (1979).
- [47] O. Lopez-Sanchez, D. Lembke, M. Kayci, A. Radenovic and A. Kis, *Nat Nano* **8** (7), 497-501 (2013).
- [48] C. Zhang, S. Wang, L. Yang, Y. Liu, T. Xu, Z. Ning, A. Zak, Z. Zhang, R. Tenne and Q. Chen, *Applied Physics Letters* **100** (24), 243101 (2012).
- [49] M. Bernardi, M. Palummo and J. C. Grossman, *Nano Letters* **13** (8), 3664-3670 (2013).
- [50] W. Ho, J. C. Yu, J. Lin, J. Yu and P. Li, *Langmuir* **20** (14), 5865-5869 (2004).
- [51] C. Cong, J. Shang, X. Wu, B. Cao, N. Peimyoo, C. Qiu, L. Sun and T. Yu, *Advanced Optical Materials* **2** (2), 131-136 (2014).
- [52] N. Peimyoo, J. Shang, C. Cong, X. Shen, X. Wu, E. K. L. Yeow and T. Yu, *ACS Nano* **7** (12), 10985-10994 (2013).
- [53] C. G. Morales-Guio, L.-A. Stern and X. Hu, *Chemical Society Reviews*



THE HONG KONG POLYTECHNIC UNIVERSITY

- 43** (18), 6555-6569 (2014).
- [54] E. Petryayeva and U. J. Krull, *Analytica Chimica Acta* **706** (1), 8-24 (2011).
- [55] E. Hutter and J. H. Fendler, *Advanced Materials* **16** (19), 1685-1706 (2004).
- [56] Y. Chen and H. Ming, *Photonic Sens* **2** (1), 37-49 (2012).
- [57] S. Underwood and P. Mulvaney, *Langmuir* **10** (10), 3427-3430 (1994).
- [58] P. Mulvaney, *Langmuir* **12** (3), 788-800 (1996).
- [59] X. Qu, Z. Peng, X. Jiang and S. Dong, *Langmuir* **20** (7), 2519-2522 (2004).
- [60] K. Jia, M. Y. Khaywah, Y. Li, J. L. Bijeon, P. M. Adam, R. D eturche, B. Guelorget, M. Fran ois, G. Louarn and R. E. Ionescu, *ACS Applied Materials & Interfaces* **6** (1), 219-227 (2014).
- [61] G. Mie, *Annalen der Physik* **330** (3), 377-445 (1908).
- [62] L. Zhao, K. L. Kelly and G. C. Schatz, *The Journal of Physical Chemistry B* **107** (30), 7343-7350 (2003).
- [63] S. Link and M. A. El-Sayed, *TRPC* **19** (3), 409-453 (2000).
- [64] C. F. Bohren and D. R. Huffman, in *Absorption and Scattering of Light by Small Particles* (Wiley-VCH Verlag GmbH, 2007), pp. 1-11.
- [65] A. C. Templeton, J. J. Pietron, R. W. Murray and P. Mulvaney, *The Journal of Physical Chemistry B* **104** (3), 564-570 (2000).
- [66] W. Rechberger, A. Hohenau, A. Leitner, J. R. Krenn, B. Lamprecht and F. R. Aussenegg, *Optics Communications* **220** (1-3), 137-141 (2003).
- [67] T. Atay, J.-H. Song and A. V. Nurmikko, *Nano Letters* **4** (9), 1627-1631 (2004).



THE HONG KONG POLYTECHNIC UNIVERSITY

- [68] L. Gunnarsson, T. Rindzevicius, J. Prikulis, B. Kasemo, M. Käll, S. Zou and G. C. Schatz, *The Journal of Physical Chemistry B* **109** (3), 1079-1087 (2005).
- [69] B. Lamprecht, G. Schider, R. T. Lechner, H. Ditlbacher, J. R. Krenn, A. Leitner and F. R. Aussenegg, *Physical Review Letters* **84** (20), 4721-4724 (2000).
- [70] S. A. Maier, M. L. Brongersma, P. G. Kik and H. A. Atwater, *Physical Review B* **65** (19), 193408 (2002).
- [71] J. Aizpurua, G. W. Bryant, L. J. Richter, F. J. García de Abajo, B. K. Kelley and T. Mallouk, *Physical Review B* **71** (23), 235420 (2005).
- [72] F. J. García de Abajo and A. Howie, *Physical Review Letters* **80** (23), 5180-5183 (1998).
- [73] H. Xu and M. Käll, *Physical Review Letters* **89** (24), 246802 (2002).
- [74] D. A. Genov, A. K. Sarychev, V. M. Shalaev and A. Wei, *Nano Letters* **4** (1), 153-158 (2004).
- [75] H. Tamaru, H. Kuwata, H. T. Miyazaki and K. Miyano, *Applied Physics Letters* **80** (10), 1826-1828 (2002).
- [76] C. E. Talley, J. B. Jackson, C. Oubre, N. K. Grady, C. W. Hollars, S. M. Lane, T. R. Huser, P. Nordlander and N. J. Halas, *Nano Letters* **5** (8), 1569-1574 (2005).
- [77] R. Ruppin, *Physical Review B* **26** (6), 3440-3444 (1982).
- [78] M. Schmeits and L. Dambly, *Physical Review B* **44** (23), 12706-12712 (1991).
- [79] A. V. Vagov, A. Radchik and G. B. Smith, *Physical Review Letters* **73** (7),



THE HONG KONG POLYTECHNIC UNIVERSITY

1035-1038 (1994).

- [80] A. V. Radchik, A. V. Paley, G. B. Smith and A. V. Vagov, *Journal of Applied Physics* **76** (8), 4827-4835 (1994).
- [81] G. B. Smith, W. E. Vargas, G. A. Niklasson, J. A. Sotelo, A. V. Paley and A. V. Radchik, *Optics Communications* **115** (1-2), 8-12 (1995).
- [82] J. J. Xiao, J. P. Huang and K. W. Yu, *Physical Review B* **71** (4), 045404 (2005).
- [83] F. J. García de Abajo, *Physical Review Letters* **82** (13), 2776-2779 (1999).
- [84] A. A. Lalayan, K. S. Bagdasaryan, P. G. Petrosyan, K. V. Nerkararyan and J. B. Ketterson, *Journal of Applied Physics* **91** (5), 2965-2968 (2002).
- [85] P. Nordlander, C. Oubre, E. Prodan, K. Li and M. I. Stockman, *Nano Letters* **4** (5), 899-903 (2004).
- [86] T. S. Sreeprasad, P. Nguyen, N. Kim and V. Berry, *Nano Letters* **13** (9), 4434-4441 (2013).
- [87] M. A. Lukowski, A. S. Daniel, C. R. English, F. Meng, A. Forticaux, R. J. Hamers and S. Jin, *Energy & Environmental Science* **7** (8), 2608-2613 (2014).
- [88] J. Kim, S. Byun, A. J. Smith, J. Yu and J. Huang, *The Journal of Physical Chemistry Letters* **4** (8), 1227-1232 (2013).
- [89] C. Xu, X. Wang and J. Zhu, *The Journal of Physical Chemistry C* **112** (50), 19841-19845 (2008).
- [90] R. Muszynski, B. Seger and P. V. Kamat, *The Journal of Physical Chemistry C* **112** (14), 5263-5266 (2008).
- [91] P. V. Kamat, *The Journal of Physical Chemistry Letters* **1** (2), 520-527



THE HONG KONG POLYTECHNIC UNIVERSITY

- (2010).
- [92] C. Shahar, R. Levi, S. R. Cohen and R. Tenne, *The Journal of Physical Chemistry Letters* **1** (2), 540-543 (2010).
- [93] W. Zhang, D. Demydov, M. P. Jahan, K. Mistry, A. Erdemir and A. P. Malshe, *Wear* **288** (0), 9-16 (2012).
- [94] B. Govinda Rao, H. S. S. R. Matte and C. N. R. Rao, *J Clust Sci* **23** (3), 929-937 (2012).
- [95] Q. He, Z. Zeng, Z. Yin, H. Li, S. Wu, X. Huang and H. Zhang, *Small* **8** (19), 2994-2999 (2012).
- [96] F. A. Frame and F. E. Osterloh, *The Journal of Physical Chemistry C* **114** (23), 10628-10633 (2010).
- [97] D. Voiry, H. Yamaguchi, J. Li, R. Silva, D. C. B. Alves, T. Fujita, M. Chen, T. Asefa, V. B. Shenoy, G. Eda and M. Chhowalla, *Nat Mater* **12** (9), 850-855 (2013).
- [98] A. Tanaka, N. J. Watkins and Y. Gao, *Physical Review B* **67** (11), 113315 (2003).
- [99] S. Najmaei, A. Mlayah, A. Arbouet, C. Girard, J. Léotin and J. Lou, *ACS Nano* **8** (12), 12682-12689 (2014).
- [100] Y. Sun, K. Liu, X. Hong, M. Chen, J. Kim, S. Shi, J. Wu, A. Zettl and F. Wang, *Nano Letters* **14** (9), 5329-5334 (2014).
- [101] U. Bhanu, M. R. Islam, L. Tetard and S. I. Khondaker, *Sci. Rep.* **4** (2014).
- [102] Y. Shi, J.-K. Huang, L. Jin, Y.-T. Hsu, S. F. Yu, L.-J. Li and H. Y. Yang, *Sci. Rep.* **3** (2013).
- [103] T. L. Jennings, M. P. Singh and G. F. Strouse, *Journal of the American*



THE HONG KONG POLYTECHNIC UNIVERSITY

- Chemical Society **128** (16), 5462-5467 (2006).
- [104] S. Mouri, Y. Miyauchi and K. Matsuda, *Nano Letters* **13** (12), 5944-5948 (2013).
- [105] N. Peimyoo, W. Yang, J. Shang, X. Shen, Y. Wang and T. Yu, *ACS Nano* (2014).
- [106] M. Achermann, *The Journal of Physical Chemistry Letters* **1** (19), 2837-2843 (2010).
- [107] M. Yi and Z. Shen, *Journal of Materials Chemistry A* **3** (22), 11700-11715 (2015).
- [108] D. M. Mattox, in *Handbook of Physical Vapor Deposition (PVD) Processing*, edited by D. M. Mattox (William Andrew Publishing, Westwood, NJ, 1998), pp. 56-126.
- [109] K. S. Sree Harsha, in *Principles of Vapor Deposition of Thin Films*, edited by K. S. S. Harsha (Elsevier, Oxford, 2006), pp. 453-533.
- [110] D. M. Mattox, in *Handbook of Physical Vapor Deposition (PVD) Processing*, edited by D. M. Mattox (William Andrew Publishing, Westwood, NJ, 1998), pp. 343-405.
- [111] D. M. Mattox, in *Handbook of Physical Vapor Deposition (PVD) Processing*, edited by D. M. Mattox (William Andrew Publishing, Westwood, NJ, 1998), pp. 288-342.
- [112] S. J. B. Reed, *Journal of Microscopy* **193** (3), 268-268 (1999).
- [113] in *Encyclopedia of Biophysics*, edited by G. K. Roberts (Springer Berlin Heidelberg, 2013), pp. 102-102.
- [114] K. J. Klabunde, in *Nanoscale Materials in Chemistry* (John Wiley & Sons,



THE HONG KONG POLYTECHNIC UNIVERSITY

- Inc., 2002), pp. 1-13.
- [115] J. Gooch, in *Encyclopedic Dictionary of Polymers*, edited by J. Gooch (Springer New York, 2011), pp. 759-759.
- [116] in *Encyclopedia of Genetics, Genomics, Proteomics and Informatics* (Springer Netherlands, 2008), pp. 1632-1632.
- [117] in *Dictionary Geotechnical Engineering/Wörterbuch GeoTechnik* (Springer Berlin Heidelberg, 2014), pp. 989-989.
- [118] W. Plieth, in *Spectroscopic and Diffraction Techniques in Interfacial Electrochemistry*, edited by C. Gutiérrez and C. Melendres (Springer Netherlands, 1990), Vol. 320, pp. 223-260.
- [119] K. Okitsu, in *UV-VIS and Photoluminescence Spectroscopy for Nanomaterials Characterization*, edited by C. Kumar (Springer Berlin Heidelberg, 2013), pp. 151-177.
- [120] H. Chen, X. Kou, Z. Yang, W. Ni and J. Wang, *Langmuir* **24** (10), 5233-5237 (2008).
- [121] C.-K. Tsung, X. Kou, Q. Shi, J. Zhang, M. H. Yeung, J. Wang and G. D. Stucky, *Journal of the American Chemical Society* **128** (16), 5352-5353 (2006).
- [122] A. A. Mitioglu, P. Plochocka, J. N. Jadcak, W. Escoffier, G. L. J. A. Rikken, L. Kulyuk and D. K. Maude, *Physical Review B* **88** (24), 245403 (2013).
- [123] L. Britnell, R. M. Ribeiro, A. Eckmann, R. Jalil, B. D. Belle, A. Mishchenko, Y. J. Kim, R. V. Gorbachev, T. Georgiou, S. V. Morozov, A. N. Grigorenko, A. K. Geim, C. Casiraghi, A. H. C. Neto and K. S.



THE HONG KONG POLYTECHNIC UNIVERSITY

- Novoselov, *Science* **340** (6138), 1311-1314 (2013).
- [124] A. Chernikov, T. C. Berkelbach, H. M. Hill, A. Rigosi, Y. Li, O. B. Aslan, D. R. Reichman, M. S. Hybertsen and T. F. Heinz, *Physical Review Letters* **113** (7), 076802 (2014).
- [125] V. Huard, R. T. Cox, K. Saminadayar, A. Arnoult and S. Tatarenko, *Physical Review Letters* **84** (1), 187-190 (2000).
- [126] S. Behura and V. Berry, *ACS Nano* **9** (3), 2227-2230 (2015).
- [127] H. Nan, Z. Wang, W. Wang, Z. Liang, Y. Lu, Q. Chen, D. He, P. Tan, F. Miao, X. Wang, J. Wang and Z. Ni, *ACS Nano* **8** (6), 5738-5745 (2014).
- [128] S. Butun, S. Tongay and K. Aydin, *Nano Letters* (2015).
- [129] I. Romero, J. Aizpurua, G. W. Bryant and F. J. García De Abajo, *Opt. Express* **14** (21), 9988-9999 (2006).
- [130] F. Huang and J. J. Baumberg, *Nano Letters* **10** (5), 1787-1792 (2010).
- [131] Y. Zhang, O. Pluchery, L. Caillard, A.-F. Lamic-Humblot, S. Casale, Y. J. Chabal and M. Salmeron, *Nano Letters* **15** (1), 51-55 (2014).
- [132] B. Chakraborty, A. Bera, D. V. S. Muthu, S. Bhowmick, U. V. Waghmare and A. K. Sood, *Physical Review B* **85** (16), 161403 (2012).
- [133] S. Marhaba, G. Bachelier, C. Bonnet, M. Broyer, E. Cottancin, N. Grillet, J. Lermé, J.-L. Vialle and M. Pellarin, *The Journal of Physical Chemistry C* **113** (11), 4349-4356 (2009).
- [134] Y. Kang, S. Najmaei, Z. Liu, Y. Bao, Y. Wang, X. Zhu, N. J. Halas, P. Nordlander, P. M. Ajayan, J. Lou and Z. Fang, *Advanced Materials* **26** (37), 6467-6471 (2014).
- [135] Y. Y. Hui, X. Liu, W. Jie, N. Y. Chan, J. Hao, Y.-T. Hsu, L.-J. Li, W. Guo



THE HONG KONG POLYTECHNIC UNIVERSITY

and S. P. Lau, *ACS Nano* **7** (8), 7126-7131 (2013).

[136] M. Buscema, G. Steele, H. J. van der Zant and A. Castellanos-Gomez,
Nano Res. **7** (4), 561-571 (2014).

[137] D. E. Eastman, *Physical Review B* **2** (1), 1-2 (1970).